UNIVERSIDADE DE COIMBRA

Study of ATLAS sensitivity to the single top s-channel production

Dissertação submetida para a obtenção do Grau de Mestre em Física Nuclear e de Partículas

Susana Patrícia Amor dos Santos

Orientador: Professor Doutor João Carlos Lopes Carvalho

Co-Orientador: Professor Doutor António Joaquim Onofre de A. R. Gonçalves

Coimbra, 2010

"In physics, one discovery often leads to others. Top opens a new world – the domain of a very heavy fermion – in which the strange and wonderful may greet us."

Chris Quigg

Resumo

A produção de *single top* pode ser dividida em três mecanismos diferentes, cada um com o seu próprio estado final distinto, topologia e fundo. No LHC, estes eventos irão ser produzidos com cerca de um terço da taxa de produção dos pares de quarks top. Além disso, a determinação precisa das secções eficazes correspondentes é sensível a física para além do Modelo Padrão, sugerindo o quark top como um lugar privilegiado para a procura de "nova física".

Nesta tese, realizou-se o estudo da sensibilidade da experiência ATLAS, no LHC, à medida da secção eficaz do processo de produção simples de quarks top através do canal-s, para uma luminosidade integrada de $200\,\mathrm{pb}^{-1}$. De modo a simular o período de dados inicial do LHC, recorreu-se à simulação completa (FullSim) do detector a uma energia de centro-de-massa de $\sqrt{s} = 7\,\mathrm{TeV}$. Os eventos de sinal foram gerados pelo gerador MC@NLO, bem como a maioria dos eventos de fundo. Os restantes fundos foram gerados usando o gerador ALPGEN ou o HERWIG. A selecção de eventos de canal-s de *single top* foi desenvolvida numa análise sequencial e discriminante, de modo a maximizar a eficiência de selecção de sinal e a rejeição de fundo. A partir dos resultados obtidos, foi possível estabelecer um limite para a secção eficaz de produção do canal-s a um nível de confiança de 95%.

Abstract

The single top production can be divided into three different mechanisms, each with its own distinct final state topology and background. At the LHC, these events will be produced at about a third of the rate of top quark pairs. Moreover, the precise determination of the corresponding cross sections is sensitive to physics beyond the Standard Model, suggesting the top quark as an excelent place to look for 'new physics'.

In this thesis, the sensitivity of the LHC ATLAS experiment to the measurement of the single top s-channel process cross section, for a low luminosity of $200\,\mathrm{pb}^{-1}$ of data, was studied. In order to simulate the early data period of LHC, the full simulation (FullSim) of the detector was used, at a center-of-mass energy of $\sqrt{s} = 7\,\mathrm{TeV}$. The signal events were generated by the MC@NLO generator, as well as most of the background events. The other background samples were generated using either ALPGEN or HERWIG. The selection of the single top quark events was developed in a sequencial and a discriminant analysis, maximizing the efficiency of event selection and background rejection. From the obtained results, a limit on the single top s-channel production process was estabilished at 95% Confidence Level.

Acknowledgements

First of all, I would like thank my supervisors, Professors António Onofre and João Carvalho, for their exceptional guidance and support. Their friendship and professional collaboration meant a great deal to me. I would also like to thank all the help and dedication of Nuno Castro, Filipe Veloso and Rita Monteiro. All those conversations kept this thesis in motion. I am also thankful to Professor Orlando Oliveira for the suggestions given in the Theoretical Framework chapter of this thesis.

I am deeply indebted to Inês Ochoa, who embarked with me in this physical journey from the beginning. Thank you for your help, for your patience and, most of all, for your friendship.

To my new Coimbra family, Pedro, Nuno, Raquel, Galhardo, Diana, João, "Mortágua", Agatão and "Mamede", thank you, for all the late meals, working nights and the other not so working nights! I also have to thank all my physicist friends, in particular to Gafeira, Márcio, Tiago and Edward, who were as nervous as I was on our first day in Coimbra. Special thanks to Patrícia, for welcoming me into academic life so gracefully. I also thank my girls, Mafy and Xana, for taking my mind off physics every once in a while.

My deepful thanks to my long term friends, Andreia, Sofia, Diana, Francisco, Guilherme, João A., João C., Lena, Rute, Sílvia L. and Sílvia S. for their presence and support in the good and not so good moments.

To Miguel, whose constant support, devotion and patience never ended, no words can express my greatest gratitude. You were there when you could and even when you couldn't. Thank you.

Finally, I am truly grateful to my parents, who always showed me the way and helped me through it. To my little sister, Ana, my beacon of light, thank you!

I acknowledge the support given by Fundação para a Ciência e Tecnologia, through the projects CERN/FP/83588/2008, CERN/FP/83551/2008 and CERN/FP/109309/2009.

Contents

List of Figures

List of Tables

Chapter 1

Introduction

In nature, there are six known quarks: the up, the down, the charm, the strange, the top and the bottom quark. According to the Standard Model (SM), they are arranged in three generations. The charged-current weak interaction allows the transformation of an up-type quark into its partner. There are also three known lepton families, which, together with the quarks, complete all the known luminous matter in the Universe. Therefore, the understanding of the properties of the quarks and leptons and their interactions is extremely important.

The top quark is the most recently discovered quark [1, 2], which was observed in 1995 by the CDF and D0 experiments at the Fermilab Tevatron. Its discovery as the weak-isospin partner of the b-quark proved the Standard Model predictions made in 1973 by Kobayashi and Maskawa [3]. The top quark is the heaviest known quark, with a mass near the scale of electroweak symmetry breaking. Thus, it is a natural candidate to test physics beyond the SM. So far, the SM predictions on top quark physics have been verified by the Tevatron results; however, the precision of its measurements leaves room for improvement.

In spite of its relatively recent discovery, far more is known about the top quark than about the other quarks. The top quark decays almost exclusively to a bW, both on-shell, due to the large top mass. Since the mean hadronization time is $\sim 10^{-24}$ s and its lifetime is of the order of 10^{-25} s, the top quark decays before hadronization takes place. Hence, unlike all the other lighter

quarks, the top quark does not have time to form bound states. Moreover, its spin and momentum information are transfered to the decay products, allowing the detailed study of the Wtb vertex and the top production mechanism. As a result, the top quark physics is independent of many of the complex consequences of hadronization, as opposed to any other quark.

There is still a lot to learn on the top quark strong and weak interactions. There are two top quark production mechanisms, depending on the interaction responsible for it: the top quark pair production and the single top quark production. The strong interaction is responsible for the first process, while the weak interaction leads to the second one. The single top production mechanism has a lower cross section and can be divided into three different channels: the t-channel, the Wt associated production and the s-channel. While the $t\bar{t}$ process was first observed at the Fermilab by the CDF and D0 experiments in 1995 [1, 2], single top (t+s channels) discovery occured in December 2006 by the D0 experiment [4] and was later confirmed by CDF in 2008 [5]. In the single top channels no measurements were made, aside the cross sections, due to the very low statistics available at Tevatron.

The Large Hadron Collider (LHC), a proton-proton collider with an expected energy of 7 TeV per beam and an integrated luminosity of 10 fb^{-1} per year and per experiment, will be a "top factory", producing around 8 million $t\bar{t}$ pairs and another few million single top events. The LHC is operating since March 2010 at a current center of mass energy of $\sqrt{s} = 7\,\text{TeV}$. The amount of data obtained by the LHC experiments will enable the precise measurement of the top quark properties as well as a detailed study of its strong and weak interactions.

In the present thesis, the leptonic s-channel single top quark production was studied, at 3.5 TeV per beam and an integrated luminosity of $200\,\text{pb}^{-1}$ with simulated data. The study was divided into a sequential and a discriminant analysis, in order to maximize the signal to background ratio. After the analysis, a limit on the cross section of the single top s-channel production was made with a 95% CL at 7 TeV.

This thesis is organized as follows. In chapter 2, a brief review of the Standard Model and the top quark is presented. The LHC and the ATLAS experiment are discussed in chapter 3, followed by a description of the Monte

Carlo generation and simulation of signal and background events, in chapter 4. The event analysis is discussed in chapter 5. In chapter 6 a limit on the cross section is calculated and finally, in chapter 7, some conclusions are drawn.

Chapter 2

Theoretical Framework

The Standard Model (SM) of particle physics is a gauge theory that describes the elementary particles and three known fundamental interactions through which they can interact[1]. It has been successful in the description of the available particle physics experimental data, nevertheless, it might be valid only at the presently accessible range of energies and therefore is unlikely to be a final theory. In this chapter, the Standard Model is briefly discussed, as well as the theoretical aspects relevant to the present study. The top quark is discussed in section 2.2, with emphasis on its properties, decay modes and mechanisms of production at the LHC, in particular, the single top quark production.

2.1 The Standard Model

Quantum field theory combines quantum mechanics and relativity, providing a theoretical framework for constructing quantum mechanical models of systems classically described by fields. Initially the Standard Model [6] was simply an electroweak theory based on the gauge group $SU(2)_L \times U(1)_Y$ proposed by Glashow [7], Salam [8] and Weinberg [9], which unified the weak and the electromagnetic interactions. In order to describe the Strong Interaction, a $SU(3)$ symmetry group was used in a similar fashion, leading to Quantum Chromodynamics theory (QCD). Thus, the SM comprises

[1]The gravity force cannot be discribed by the SM yet.

a relativistic quantum field theory based on a set of fields and gauge symmetries ($SU(3)_C \times SU(2)_L \times U(1)_Y$), which accurately describes the known phenomenology [10].

The Standard Model divides matter into fermions and bosons according to whether or not they respect the Pauli exclusion principle. There are twelve known fundamental fermions in the SM and their respective antiparticles. The fermions are particles of spin $\frac{1}{2}$, which obey the Pauli Exclusion Principle. They are classified as quarks (up, down, charm, strange, top, bottom) and as leptons (electron, muon, tau, and their corresponding neutrinos). Since quarks hold color charge, electric charge and weak isospin, they can interact via the strong and electroweak interaction. Quarks are believed to form color-neutral particles called hadrons, which are divided into baryons (three quarks systems) and mesons (quark-antiquark systems). On the other hand, leptons are colorless, so they only interact through the electroweak force. Since neutrinos are electrically neutral they can only interact via weak interactions.

The bosons have integer spin and obey the Bose-Einstein statistics. The Standard Model predicts four gauge bosons (photons, gluons, $W^{\pm}$, Z) and one higgs boson (Φ). The photons are massless particles and mediate the electromagnetic interaction. The massive gauge bosons, $W^{\pm}$ and Z particles, together with the photons, constitute the mediating particles of the electroweak interaction. The Z boson is electrical neutral and has a higher mass than the W bosons ($m_W = 80.398 \pm 0.025 \mathrm{GeV/c^2}$ and $m_Z = 91.1876 \pm 0.0021 \mathrm{GeV/c^2}$) [6]. Finally, the gluons are responsible for mediating the strong force. According to quantum chromodynamics there are eight gluons, which have zero mass and are color charged, which allows them to interact amongst themselves. They are responsible for the strong interaction between quarks, which exist in three color versions : red, green or blue.

Having defined the gauge symmetries and specified the fields, the Lagrangian of the Standard Model is fixed by requiring it to be gauge invariant, local, and renormalisable. The Standard Model Lagrangian[2], $\mathcal{L}_{SM}$, can be divided in four parts:

$$\mathcal{L}_{SM} = \mathcal{L}_{Gauge} + \mathcal{L}_{Matter} + \mathcal{L}_{Higgs} + \mathcal{L}_{Yukawa} \tag{2.1}$$

[2]Whenever mentioning the lagrangian, one is actually refering to the lagrangian density.

The first part is the pure Gauge Lagrangian and is given by :

$$\mathcal{L}_{Gauge} = -\underbrace{\frac{1}{4}G_a^{\mu\nu}G^a_{\mu\nu}}_{SU(3)} - \underbrace{\frac{1}{4}W_i^{\mu\nu}W^i_{\mu\nu}}_{SU(2)} - \underbrace{\frac{1}{4}B^{\mu\nu}B_{\mu\nu}}_{U(1)}, \tag{2.2}$$

with

$$G^a_{\mu\nu} = \partial_\mu G^a_\nu - \partial_\nu G^a_\mu - g_S f^{abc} W^b_\mu W^c_\nu, \tag{2.3}$$

$$W^i_{\mu\nu} = \partial_\mu W^i_\nu - \partial_\nu W^i_\mu - g\epsilon^{ijk} W^j_\mu W^k_\nu, \tag{2.4}$$

$$B_{\mu\nu} = \partial_\mu B_\nu - \partial_\nu B_\mu. \tag{2.5}$$

where $a = 1,...,8$ and $i = 1,...,3$ are the $SU(2)$ and $SU(3)$ indices respectively. The $G^{\mu\nu}_a$, $W^{\mu\nu}_i$ and $B^{\mu\nu}$ are the gluon, weak and hypercharge field-strength tensors. The hypercharge operator $\hat{Y}$ is the generator of $U(1)$ and the generator of $SU(2)$ is the weak isospin operator $\hat{T}$. The constants g and g' correspond to the electroweak gauge couplings, whereas g_S is the strong gauge coupling constant. The Gauge Lagrangian contains the kinetic energy of the gauge fields as well as their self interactions. The electric charge is related with the hypercharge (Y) and the third component of weak isospin (T_3) as:

$$Q = \frac{1}{2}Y + T_3\,. \tag{2.6}$$

The second part of $\mathcal{L}_{SM}$ is the Matter Lagragian. It includes the kinetic energy of the fermions and their interactions with the gauge fields:

$$\mathcal{L}_{Matter} = \mathrm{i}\bar{Q}^i_L \not{D} Q^i_L + \mathrm{i}\bar{u}^i_R \not{D} u^i_R + \mathrm{i}\bar{d}^i_R \not{D} d^i_R + \mathrm{i}\bar{L}^i_L \not{D} L^i_L + \mathrm{i}\bar{e}^i_R \not{D} e^i_R\,, \tag{2.7}$$

where the index $i = 1, 2, 3$ labels the three generations of quarks and leptons, $\not{D} = \gamma^\mu D_\mu$ is the covariant derivative, and Q^i_L, u^i_R, d^i_R, L^i_L and e^i_R are the fermions fields. Notice that the sum over i is implied in the lagrangian. Since the field Q^i_L represents quarks, which can interact both via electroweak and strong interactions, its covariant derivative is given by:

$$\not{D} Q^i_L = \gamma^\mu \left(\partial_\mu + \frac{\mathrm{i}}{2} g_S \lambda^a G^a_\mu + \frac{\mathrm{i}}{2} g \tau^i W^i_\mu + \frac{\mathrm{i}}{2} g' Y B_\mu\right) Q^i_L\,. \tag{2.8}$$

where the λ^a are the Gell-Mann matrices and τ^i are the Pauli matrices.

The previous two parts of the $\mathcal{L}_{SM}$ only depend on the gauge couplings, whose approximate values, evaluated at M_Z, are

$$\begin{array}{rcl} g_S & \approx & 1 \\ g & \approx & 2/3 \\ g' & \approx & 2/(3\sqrt{3})\,. \end{array} \tag{2.9}$$

The matter fields, associated to quarks and leptons of spin 1/2, are discribed in terms of chiral components. In other words, the fermion fields constitute multiplets classified according to helicity states. The left handed (L) doublets of $SU(2)$:

$$L_L^i = \begin{pmatrix} \nu_e \\ e \end{pmatrix}_L \begin{pmatrix} \nu_\mu \\ \mu \end{pmatrix}_L \begin{pmatrix} \nu_\tau \\ \tau \end{pmatrix}_L \text{(for leptons)} \tag{2.10}$$

$$Q_L^i = \begin{pmatrix} u \\ d \end{pmatrix}_L \begin{pmatrix} c \\ s \end{pmatrix}_L \begin{pmatrix} t \\ b \end{pmatrix}_L \text{(for quarks)} \tag{2.11}$$

and the right handed (R) singlets of U(1) :

$$e_R^i = e_R \quad \mu_R \quad \tau_R \quad \text{(for charged leptons)} \tag{2.12}$$

$$u_R^i = u_R \quad c_R \quad t_R \quad \text{(for up-type quarks)} \tag{2.13}$$

$$d_R^i = d_R \quad s_R \quad b_R \quad \text{(for down-type quarks)} \tag{2.14}$$

The R (L) index stands for the right (left) handness of the fermions and the i index runs over the number of fermion generations. Table 2.1 summarizes the fermion fields of the Standard Model and their gauge quantum numbers (electroweak charges Q, Y and third component of weak isospin, T_3).

In spite of having a free number of fermion generations, the SM must have equal number of quark and lepton families. That is a pre-requisite of the renormalizability of the theory, so that the possible gauge anomalies in higher order calculations cancel [11].

Neither $\mathcal{L}_{Gauge}$ nor $\mathcal{L}_{Matter}$ include mass terms for fermions and bosons. The introduction of boson mass terms directly in the lagrangian would explicity break the local gauge invariance. However, the gauge bosons can acquire

	ν_L^e	e_L^-	e_R^-	u_L	d_L	u_R	d_R
Q	0	-1	-1	2/3	-1/3	2/3	-1/3
T_3	1/2	-1/2	0	1/2	-1/2	0	0
Y	-1	-1	-2	1/3	1/3	4/3	-2/3

Table 2.1: *The quantum numbers of the Standard Model fermions are shown. To each fermion corresponds an anti-particle with opposite charge, but the same mass. The electric charges, Q, are normalized to the positron charge.*

mass through a mechanism of spontaneous symmetry breaking[3]. In order to do so, another term is added to the lagrangian of the Standard Model [12, 13]:

$$\mathcal{L}_{Higgs} = (D^\mu \Phi)^\dagger (D_\mu \Phi) + \mu^2 \Phi^\dagger \Phi - \lambda (\Phi^\dagger \Phi)^2 , \tag{2.15}$$

with the Higgs doublet,

$$\Phi = \begin{pmatrix} \Phi^+ \\ \Phi^0 \end{pmatrix} . \tag{2.16}$$

The propreties of Φ^+ and Φ^0 are summarized in Table 2.2. This part includes the kinetic energy of the Higgs field, its gauge interactions and the Higgs potential, shown in Figure 2.1. The quadratic term coefficient, μ^2, is the only dimensionful parameter in the $\mathcal{L}_{Higgs}$. Its sign is chosen in order to have a non-zero vacuum-expectation value of the Higgs Field, in the minima circle of the Higgs-field space:

$$< \Phi^\circ >= \frac{\mu}{\sqrt{2\lambda}} \equiv \frac{v}{\sqrt{2}} . \tag{2.17}$$

The inclusion of this mechanism in the SM leads to the prediction of a massive scalar boson, the Higgs boson, which is yet to be discovered.

The Higgs non-zero vacuum-expectation value breaks the electroweak symmetry, generating mass terms for the $W^\pm$ and Z bosons:

$$M_W = \tfrac{1}{2} g v \quad ; \quad M_Z = \tfrac{1}{2} \sqrt{g^2 + g'^2}\, v \tag{2.18}$$

[3]Which is permited, since the spontaneous symmetry break does not spoils the renormalizabity.

Higgs Field Components	T_3	Q
Φ^+	$+1/2$	$+1$
Φ^0	$-1/2$	0

Table 2.2: *The Higgs Field quantum numbers.*

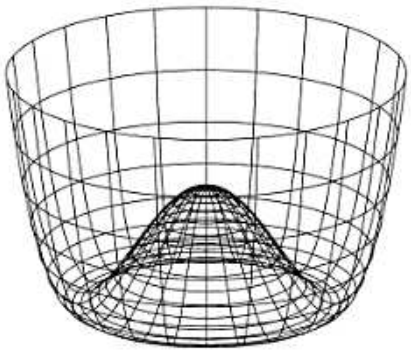

Figure 2.1: *The Higgs potential. In the Higgs-field space, the neutral component of* Φ *has the vacuum-expectation value* $<\Phi^\circ>= v/\sqrt{2}$ *on the circle of minima.*

Such mechanism is often referred in the literature as the Higgs mechanism.

The last part of the SM langragian is the Yukawa interaction of the Higgs field with the fermions, given by:

$$\mathcal{L}_{Yukawa} = -\Gamma_u^{ij}\bar{Q}_L^i\epsilon\Phi^* u_R^j - \Gamma_d^{ij}\bar{Q}_L^i\Phi d_R^j - \Gamma_e^{ij}\bar{L}_L^i\Phi e_R^j + h.c.\,, \tag{2.19}$$

with Γ_u^{ij}, Γ_d^{ij} and Γ_e^{ij} 3×3 complex matrices in the generation space, which include most of the SM parameters. Since these matrices do not need to be diagonal, there is usually mixing between different fermion families. The total antisymmetric tensor, ϵ, can be related with the second Pauli matrix, τ_2, according to:

$$\epsilon = \mathrm{i}\tau_2 \tag{2.20}$$

and ensures that each term is electrically neutral.

The fermionic mass terms are now obtained from the spontaneous symmetry breaking:

$$M_f \;=\; \Gamma_t\tfrac{v}{\sqrt{2}} \tag{2.21}$$

where Γ_t is the Yukawa coupling.

The non vanishing vacuum-expectation value of the Higgs field originates different mass eigenstates for quarks and leptons. The masses of the Standard Model fermions are shown in Table 2.3. [4] The neutrino masses are very small when compared with the quark ones. Notice that according to the SM, there are no right handed neutrinos and therefore they are expected to be massless. However, the Super-Kamiokande, K2K, SNO and KamLAND collaborations have reported evidence for neutrino oscillations, indicating that neutrinos are massive. For further information see for example [14]. The nature of neutrinos (Dirac versus Majorana) is yet to be known and is beyond the scope of this thesis.

The diagonalization of the fermion mass matrices originates the Cabibbo-Kobayashi-Maskawa (CKM) matrix which will be studied in the next subsection.

Generation	First	Second	Third
neutral leptons	ν_e	ν_μ	ν_τ
mass (MeV)	~ 0	~ 0	~ 0
charged leptons	e	μ	τ
mass (MeV)	0.511	105.66	1776.84
Up-type Quarks	u	c	t
mass (MeV)	$1.5 - 3.3$	1.27×10^3	171.2×10^3
Down-type Quarks	d	s	b
mass (MeV)	$3.5 - 6.0$	104	4.20×10^3

Table 2.3: *Table of the masses of SM fermions in MeV (values extrated from [6]).*

[4] Since quarks are confined in hadrons and are not observed as physical particles, their masses can not be directly measured. Instead, quark masses are determined indirectly through their influence in hadronic properties. Therefore, quark masses are dependent on the theoretical framework used to define it, which, in this case, is the SM.

2.1.1 The CKM quark-mixing matrix

In the Standard Model, the Yukawa interaction of quarks with the Higgs condensate originates the masses and mixings of quarks. The physical states are obtained through diagonalization of the mass matrices of the up and down quarks by four unitary matrices, $V_{L,R}^{u,d}$. The quark states can decay through weak processes, originating flavour changing currents. These charged current $W^{\pm}$ interactions couple to the up and down-type of quark fields. Assuming three families of quarks, the couplings are given by [6]:

$$V \equiv \begin{pmatrix} V_{ud} & V_{us} & V_{ub} \\ V_{cd} & V_{cs} & V_{cb} \\ V_{td} & V_{ts} & V_{tb} \end{pmatrix} \tag{2.22}$$

This 3×3 unitary matrix is the Cabibbo-Kobayashi-Maskawa (CKM) quark-mixing matrix [15, 3]. The matrix unitarity leads to only four independent parameters. A more general unitary matrix can be constructed as a product of rotation matrices and unitary matrices made up of phase factors. Using this method, there is no unique parameterisation of the CKM matrix. For instance, the Kobayashi and Maskawa parameterisation shown in the Particle Data Group [6] is:

$$V = \begin{pmatrix} c_1 & -s_1c_3 & -s_1s_3 \\ s_1c_2 & c_1c_2c_3 - s_2s_3e^{i\delta} & c_1c_2s_3 + s_2c_3e^{i\delta} \\ s_1s_2 & c_1s_2c_3 + c_2s_3e^{i\delta} & c_1s_2s_3 - c_2c_3e^{i\delta} \end{pmatrix}, \tag{2.23}$$

where $s_i = \sin\theta_i$ and $c_i = \cos\theta_i$. It uses three mixing angles (θ_1, θ_2, θ_3) and a KM phase (δ), responsible for all CP-violating phenomena in flavour changing processes in the SM.

Assuming the unitarity of the CKM matrix and the three generations SM, the allowed ranges of the magnitudes of all nine CKM elements are [6]:

$$V = \begin{pmatrix} 0.97419 \pm 0.00022 & 0.2257 \pm 0.0010 & 0.00359 \pm 0.00016 \\ 0.2256 \pm 0.0010 & 0.97334 \pm 0.00023 & 0.0415^{+0.0010}_{-0.0011} \\ 0.00874^{+0.00026}_{-0.00037} & 0.0407 \pm 0.0010 & 0.999133^{+0.000044}_{-0.000043} \end{pmatrix} \tag{2.24}$$

The weak universality relation states that the sum of all couplings of any of the up-type quarks to all the down-type quarks is the same for all

generations. This is due to the constraints of unitarity of the CKM matrix. The CKM matrix elements represent the probability of a transition from one quark to another in the $q \to q'W^{\pm}$ vertex. For instance, the $t \to Wb$ vertex transition probability is proportional, in first approximation, to $|V_{tb}|^2$. Due to the small values of V_{td} and V_{ts}, when compared with V_{tb}, the top quark decays mainly to a W boson and bottom quark. A detailed study of this vertex will be done in the next section.

2.2 The Top quark

The top quark is the up-type quark of the weak-isospin doublet containing the bottom quark, with $T_3 = +1/2$. It has an electric charge of $Q = +(2/3)|e|$ and is the heaviest known elementary particle, with a mass of $173.1 \pm 0.6(stat) \pm 1.1(syst)\mathrm{GeV/c^2}$, [16], which is about 35 times the mass of the b quark. The mass value was obtained based on published top mass measurements at the Tevatron experiments, as can be seen in Figure 2.2. This large mass value implies a Yukawa coupling to the Higgs boson with a value near unity, unlike any other known particle.

The first indirect evidence for the existence of the top quark came from the need of renormalization of the SM lagrangian, which is only possible if the sum of weak hypercharge of all left handed fermions is zero. Since the lepton multiplets contribute with $Y = -2$ and the quark multiplets with $Y = -2/3$, the sum would only vanishes if every quark existed in three colour versions and the number of quark flavours was equal to the number of lepton species. Therefore, the existence of a sixth quark seemed mandatory. In 1995, the top quark was discovered by the CDF and D0 experiments in proton-antiproton collisions ($q\bar{q} \to t\bar{t}$ and $gg \to t\bar{t}$) with a center-of-mass energy $\sqrt{s} = 1.8\mathrm{TeV}$ at the Fermilab Tevatron collider [1, 2], completing the three-generation structure of the SM.

The top quark is a very interesting particle, not only due to its very high mass, but also due to its small lifetime (decays before hadronizing). Furthermore, it can only decay through weak processes and, according to the CKM mixing matrix, dominantly to a W boson and a b quark. The top quark has a mean lifetime of $10^{-25}\,\mathrm{s}$, whereas its mean hadronization time is

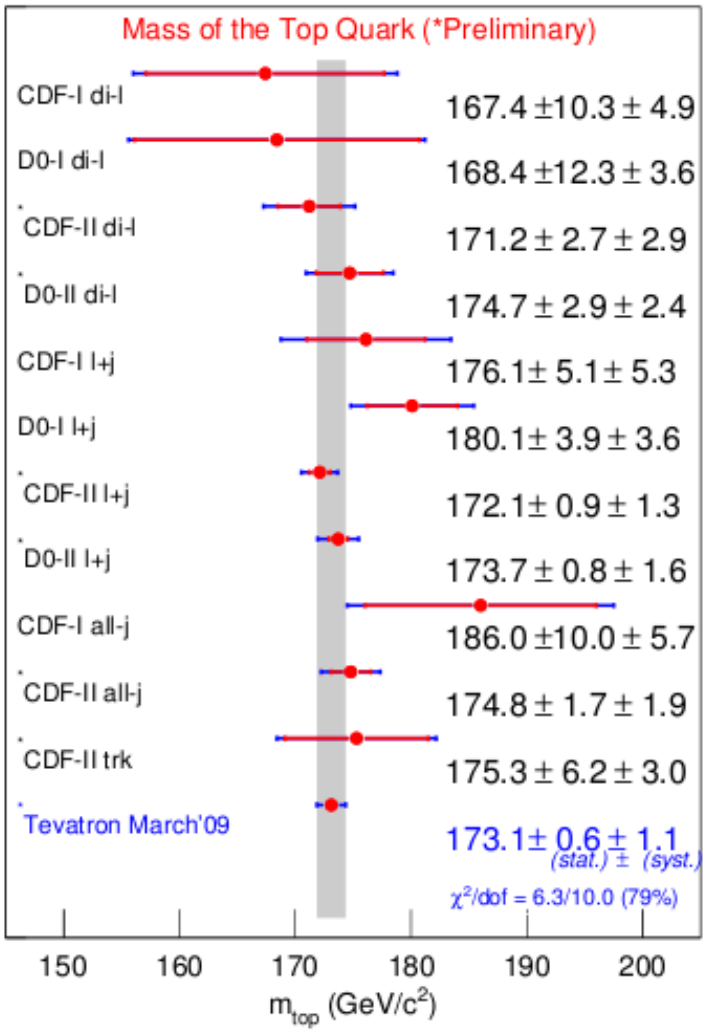

Figure 2.2: *Combined value of the measured Top quark mass at Tevatron. The individual values, from different analyses and collaborations, are also shown (extrated from Ref. [16]).*

about 10^{-24} s. This quark can be studied to a bigger extend than the others, since it is the only quark able to decay before the hadronization takes place. It allows the study of the properties of a free quark, otherwise unavailable due to the rapid hadronization of all the other flavours. The properties of the quark before the decay are then transferred into its decay products and can thus be measured to unprecedent accuracy and compared to SM predictions.

The study of the top quark is then an ideal tool for testing the SM predictions and possible new physics beyond it. The Tevatron experiments have already studied some of the top properties, at $\sqrt{s} = 1.9\,\text{TeV}$, such as its mass, width, lifetime and the production processes cross sections (for a detailed review see [17]). There were also studies of the top main decaying mode ($t \to bW$), the structure of the Wtb vertex, the measurement of the W boson helicity fractions and its rare decays through flavour changing neutral currents. However, the great majority of these studies was limited by the small statistics acquired with the Tevatron luminosity, leading to a dominant statistical contribution in the total error of these studies.

In hadron colliders, the top quark can be produced through either strong or weak mechanisms. The predominant processes of its production are the pair production (also known as $t\bar{t}$) and the single production (single top) through the strong and weak interactions, respectively. At the LHC, the QCD processes $q\bar{q} \to t\bar{t}$ and $gg \to t\bar{t}$ will be the dominant mechanisms of $t\bar{t}$ production (Figure 2.4) , with a cross section of $833^{+52}_{-39}\,\text{pb}$ [18] at 14 TeV and assuming the Standard Model at NLO (Next to Leading Order).

The single top production can occur through three different processes: the t-channel, the s-channel and the associate production (Wt-channel). The Feynman diagrams of all the three processes are shown in Figure 2.5. The expected cross sections are shown in Table 2.4 and, as can be seen, the electroweak single top quark production is less probable than the $t\bar{t}$ process. The cross sections dependency with the center-of-mass energy can be seen in Figure 2.3. The t-channel involves a space-like W boson ($q^2 \leq 0$), that strikes a b quark in the proton quark sea, originating a top quark. Since the b quark ultimately arises from a gluon, this process is also referred to as W-gluon fusion. The s-channel can be obtained from the t-channel diagram by rotating it such that the virtual W boson becomes time-like. The virtuality of the W boson is $q^2 \geq (m_t + m_b)^2$. The Wt-channel produces a single top with a real W boson ($q^2 = M_W^2$), and, as in the t-channel process, one of the initial partons is a b quark in the proton quark sea.

The pair production was first observed by the CDF and D0 experiments at $\sqrt{s} = 1.8\text{TeV}$ (in 1995 at Fermilab), with a measured cross section of $\sigma = 6.8^{+3.6}_{-2.4}\,\text{pb}$ [1] and $\sigma = 6.4 \pm 2.2\,\text{pb}$ [2], respectively. Likewise, the first

evidence for single top (t+s channels) was reported by the D0 experiment, with a cross section of $\sigma = 4.7 \pm 1.3$ pb (3.6 σ) [19]. Subsequently, the CDF experiment also measured a cross section of $\sigma = 2.2^{+0.7}_{-0.6}$ pb, assuming a top quark mass of 175 GeV [5]. The associated production will be first seen at the LHC.

$\sqrt{s}$	t-channel	s-channel	Wt-channel
7 TeV	58.73 pb	3.94 pb	13.10 pb
10 TeV	$124.5 \pm 5\%$ pb	$6.6 \pm 5\%$ pb	$32.7 \pm 5\%$ pb
14 TeV	$246^{+11.8}_{-12.2}$ pb	$10.65^{+1.12}_{-1.02}$ pb	66 ± 2 pb

Table 2.4: *The expected cross sections of the single top processes at a center-of-mass energy of* 7 *[20],* 10 *[21] and* 14 *TeV [22] [23].*

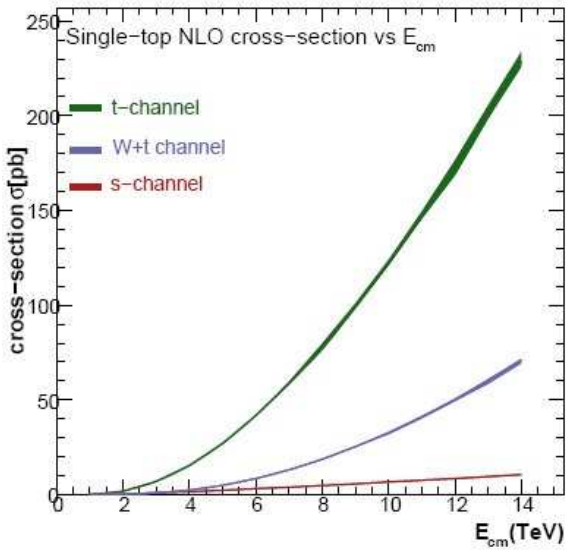

Figure 2.3: *Single top cross sections dependency with the collision center-of-mass energy (extracted from [20]).*

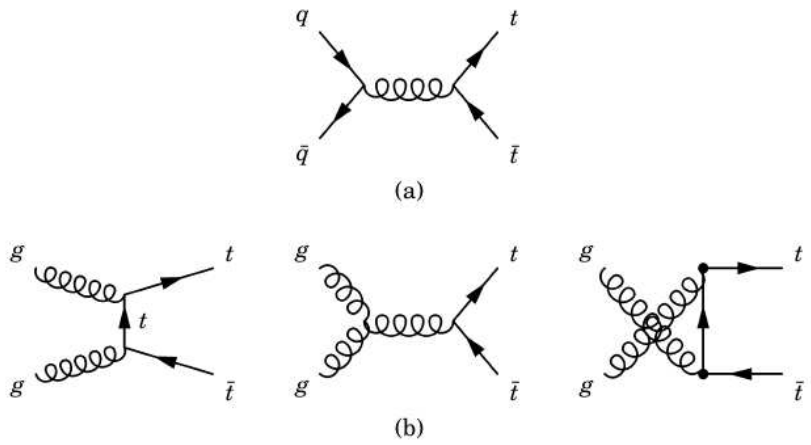

Figure 2.4: *Feynman diagrams at leading order corresponding to the $t\bar{t}$ production at the LHC: (a) quark-antiquark annihilation and (b) gluon fusion.*

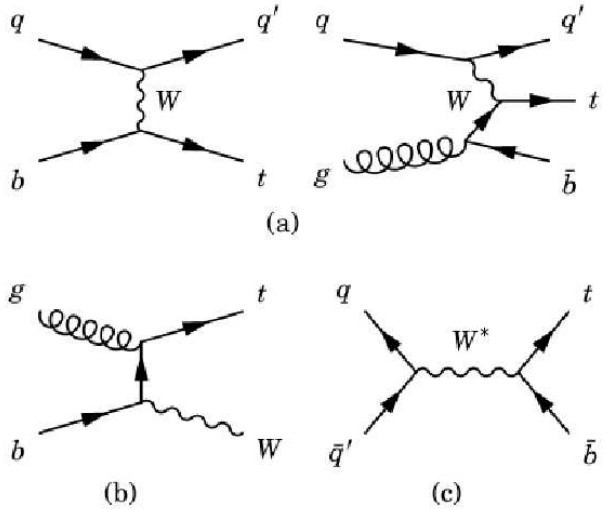

Figure 2.5: *Feynman diagrams corresponding to the single top production at the LHC: (a) t-channel; (b) Wt associated production and (c) s-channel.*

2.3 Single top quark production

2.3.1 Single top s-channel

As seen in Figure 2.5 both the t-channel and s-channel are originated in electroweak processes. The s-channel production is originated from the exchange of a charged W^* between a quark and an antiquark. Although the s-channel cross section is much lower than that of the t-channel process, the s-channel has the advantage that the quark and antiquark distribution functions are relatively well known, which leads to a small uncertainty in the parton distribution functions. Since it proceeds via the quark-antiquark annihilation, the partonic flux can be constrained from Drell-Yan data ($q\bar{q} \to l\bar{\nu}$), which also proceeds via a virtual s-channel W boson[5]. The charged W boson will then decay hadronically into a top quark and a b antiquark. According to the CKM matrix, the top quark decays mostly to a b quark and a W boson, where the W boson has $q^2 \approx M_W$. The charged boson can then decay leptonically or hadronically, dividing the single top s-channel in different final topologies.

- **Hadronic sample**: The W boson decays to a pair of quarks with a branching ratio of $67.60 \pm 0.27\%$ [6]. The final topology is $qq' \to bt \to bWb \to bjjb$.

- **Leptonic sample without taus**: The W boson decays to a lepton (an electron or a muon) and its respective neutrino with a branching ratio of $21.60 \pm 0.13\%$ [6]. The final topology is $qq' \to bt \to bWb \to bl\nu_l b$, with $l = e, \mu$.

- **Leptonic sample with taus**: The W boson decays leptonically into a tau and its respective neutrino with a branching ratio of $10.80 \pm 0.09\%$ [6]. Since the tau lepton decays dominantly to a pair of jets, the final topology is $qb \to bt \to bWb \to b\tau\nu_\tau b$

[5]Since the neutrino longitudinal momentum cannot be reconstructed, the tetramomentum of the W boson cannot be determined. The process $q\bar{q} \to l\bar{\nu}$ therefore provides a constraint on the quark-antiquark flux, not a direct measurement.

The current study is focused on the leptonic s-channel single top production (with and without taus) , whose detailed Feynman diagram can be seen in Figure 2.6. However, the W boson leptonic decays into taus are only considered as signal, when the τ decays leptonicaly. The branching ratio of the signal process is then $32,57\%$ [6]. The detailed signal analysis can be found in the fourth chapter.

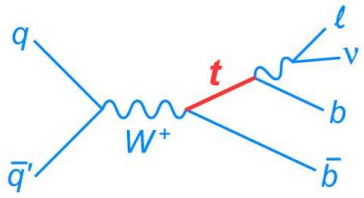

Figure 2.6: *Feynman diagram of the leptonic single top s-channel.*

The events with single top quarks can also be used to study the Wtb coupling, and to measure directly the absolute value of the CKM matrix element $|V_{tb}|$ without assuming three generations of quarks. Notice that a value not close to one would imply the existence of a fourth quark family.

2.3.2 The Wtb Vertex

In order to measure the $|V_{tb}|$ directly, without any assumptions on the number of quark generations, one simply needs to measure the cross sections of the single top quark production via the electroweak interaction. In the top decay, the square of the CKM mixing matrix elements V_{ts} and V_{td} supress the Ws and Wd final states relatively to Wb. Assuming the unitarity of the CKM matrix, these values can be estimated to be less than 0.043 and 0.014, respectively, which leads to a lower probability of occurrence of the $t \to Ws$ ($BR \sim 0.19\%$) and $t \to Wd$ ($BR \sim 0.01\%$) [17]. The branching ratio of the $t \to Wb$ process is proportional to $|V_{tb}|^2$ in first order, and so are the cross sections of the three single top processes. In addition, the size and structure of the Wtb vertex will influence the single top quark production. In the SM, this vertex is purely left-handed, and its size is given by the CKM matrix element V_{tb}. At Leading Order (LO) the width of the $t \to Wb$ vertex is given

by:

$$\Gamma_{LO}(t \to Wb) = \frac{G_F}{8\pi\sqrt{2}}|V_{tb}|^2 m_t^3 \Big(1 - 3\frac{M_W^4}{m_t^4} + 2\frac{M_W^6}{m_t^6}\Big), \tag{2.25}$$

where m_t and m_W are the top and the W boson masses, respectively. G_F is the Fermi coupling constant and it contains the largest part of the one-loop electroweak radiative corrections. Using the experimental values, the top quark width was estimated to be $\Gamma_{LO} = 1.56\,\text{GeV}$ and when taking into account higher order corrections $\Gamma_{NLO} = 1.42\,\text{GeV}$ [24].

2.3.3 Anomalous couplings

The study of the Wtb coupling can lead to new physics models. Since the CKM matrix element $|V_{tb}|$ can be measured without any assumption on the number of quark families, its measure can prove the SM predictions or, instead, demand new physic models. These models can then include a $|V_{tb}|$ different from the expected value, as well as new radiative contributions to the Wtb vertex. The Lagrangian for the onshell Wtb vertex, with terms up to dimension five [25], is given by:

$$\mathcal{L} = -\frac{g}{\sqrt{2}}\bar{b}\gamma^\mu(V_L P_L + V_R P_R)tW_\mu^- - \frac{g}{\sqrt{2}}\bar{b}\frac{i\sigma^{\mu\nu}q_\nu}{M_W}(g_L P_L + g_R P_R)tW_\mu^- + h.c. \tag{2.26}$$

where $q = p_t - p_b$ is the W boson momentum and $P_{L,R} = (1 \mp \gamma_5)$ are the helicity projectors. The $V_{L,R}$ and $g_{L,R}$ are the vector-like and tensor-like couplings, where $V_L = V_{tb} \approx 1$ according to the SM. The anomalous couplings (V_R, g_R and g_L) are related to the W boson helicity fractions and vanish at the tree level [26]. If CP conservation is assumed, they can be taken as real. According to some models beyond the SM, it is possible to have additional contributions to the anomalous couplings without spoiling the agreement with low energy measurements. Therefore, the measurement of these observables is important in the search of new physics.

2.3.4 W boson Polarization and Angular asymmetries

According to the Feynman rules, the top quark has a $(V-A)$ charged-current weak interaction similar to all the other fermions:

$$(V-A) = -\mathrm{i}\frac{g}{\sqrt{2}}V_{tb}\gamma^{\mu}\frac{1}{2}(1-\gamma_5) \tag{2.27}$$

In the top quark decay, the emitted W boson is polarized with positive, negative or zero helicity. Each polarization state has a corresponding partial width (Γ_R, Γ_L and Γ_0) defined in relation to the total width, $\Gamma(t \to W+b) = \Gamma_R + \Gamma_L + \Gamma_0$. In the limit of $m_b = 0$, the Γ_R component is zero. Since the b quark has a very small mass when compared to the other particles involved, its mass can be considered as zero. The (V-A) current implies that the massless bottom quark must be left-handed. For very high energy fermions ($m \approx 0$), the helicity and chirality assume a similar meaning, so the bottom quark produced in the $t \to Wb$ vertex must have negative helicity. In the top quark center of mass, the b quark and the W boson are emitted in opposite directions, so that the momentum is conserved (Figure 2.7). Therefore, the W boson cannot be right-handed (positive helicity), for there must be spin angular momentum conservation. That is, the sum of the b quark spin with the spin of the W boson, has to be the top quark spin angular momentum ($\pm 1/2$).

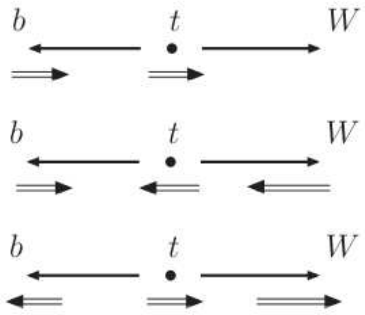

Figure 2.7: *Illustration of the W possible helicity states in the top quark rest frame. The double arrow represents the spin angular momentum of the particles and the bold arrow represents their momenta (extrated from Ref. [17]).*

The top quark can then decay to a left-handed (negative helicity) or a

longitudinal (zero helicity) W boson. According to the SM, it decays to a longitudinally polarized W boson with a probability of $\sim 70.3\%$, at leading order, and to a left-handed W boson with a probability of $\sim 29.7\%$. The suppressed right-handed state of the charged W has a probability of 0.036% [25].

The angular distribution of the W boson decay products can be determined by the different polarization states of the charged electroweak W boson. For instance, the angle between the charged lepton momentum and the bottom quark in the W rest frame, θ_l, is usefull in the study of the W polarization. The normalized angular distribution for the charged lepton is given by [25]:

$$\frac{1}{\Gamma}\frac{\mathrm{d}\Gamma}{\mathrm{d}\cos\theta_\ell^*} = \frac{3}{4}\sin^2\theta_\ell^*\, F_0 + \frac{3}{8}(1-\cos\theta_\ell^*)^2\, F_L + \frac{3}{8}(1+\cos\theta_\ell^*)^2\, F_R \qquad (2.28)$$

where F_0, F_L and F_R are the fractions of the longitudinal, left-handed and right-handed helicities, respectively. $\theta_l^* = \pi - \theta_l$ is the supplementary angle of θ_l, which is, in fact, the angle between the charged lepton momentum (in the W boson rest frame) and the W boson momentum (in the top quark rest frame). The Standard Model angular distribution depends mainly on the longitudinal and left-handed helicities contributions, due to the lower right-handed helicity fraction, as can be seen in Figure 2.8.

Angular asymmetries can now be defined, from the SM angular distribution $\Gamma(\cos\theta_\ell^*)$. These asymmetries are sensitive to the anomalous couplings and, for any fixed value of z in the interval $[-1, 1]$, they can be defined as:

$$A_z = \frac{N(\cos\theta_\ell^* > z) - N(\cos\theta_\ell^* < z)}{N(\cos\theta_\ell^* > z) + N(\cos\theta_\ell^* < z)} \qquad (2.29)$$

where N is the number of events.

According to the chosen z value, different asymmetries can be obtained. If the chosen z value is zero, the forward-backward asymmetry A_{FB} can be defined. This asymmetry is related to the W boson helicity fractions F_R and $\mathrm{F_L}$, and as so the asymmetry measurement is not enough to fully calculate the $\cos\theta_\ell^*$ distribution in equation (2.26). In order to determine the W boson helicity fractions, different values of z have to be considered. For instance, the determination of F_i is easier if asymmetries involving only F_R

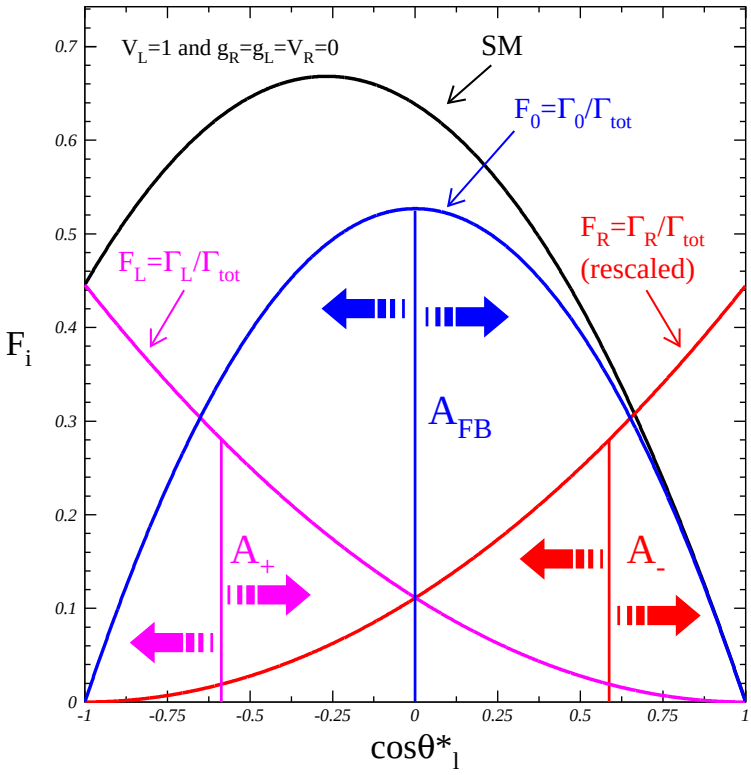

Figure 2.8: *Angular distributions and asymmetries representation on the Wtb vertex. The right-handed component of the distribution is rescaled to F_L component.*

and F_0, or F_L and F_0 are chosen. This is achieved by choosing $z = \mp(2^{2/3}-1)$:

$$z = 0 \;\rightarrow\; A_{FB} = \frac{3}{4}(F_R - F_L) = -0.223 \tag{2.30}$$

$$z = -(2^{2/3}-1) \;\rightarrow\; A_+ = 3\beta[F_0 + (1+\beta)F_R] = 0.548 \tag{2.31}$$

$$z = (2^{2/3}-1) \;\rightarrow\; A_- = -3\beta[F_0 + (1+\beta)F_L] = -0.840 \tag{2.32}$$

where $\beta = (2^{1/3}-1)$. These observables were calculated with the SM distribution at leading order. As can be seen, the forward-backward asymmetry, A_{FB}, is insensitive to the longitudinal fraction and the chosen β value leads to A_+ and A_- that are not sensitive to the left-handed and right-handed helicities, respectively.

The presence of anomalous couplings will modify the helicity fractions of the W boson with respect to their SM values. The Figures 2.9 and 2.10 show the dependence of the helicity fractions and angular asymmetries on the anomalous couplings. In each curves only one coupling is considered different from zero and the CP-conserving case of real V_R, g_R and g_L is assumed. The depence on the Wtb anomalous couplings on the partial widths, corresponding to the three W boson helicities, are (Ref. [25]):

$$\begin{aligned} F_0 \;=\; & \frac{1}{\Gamma}\frac{g^2|\vec{q}|}{32\pi}\left\{ \frac{m_t^2}{M_W^2}\left[V_L^2+V_R^2\right]\left(1-x_W^2-2x_b^2-x_W^2x_b^2+x_b^4\right)\right. \\ & +\left[g_L^2+g_R^2\right]\left(1-x_W^2+x_b^2\right)-4x_b\left[V_LV_R+g_Lg_R\right] \\ & -2\frac{m_t}{M_W}V_L\left[g_R-x_bg_L\right]\left(1-x_b^2\right)-2\frac{m_t}{M_W}V_R\left[g_L-x_bg_R\right]\left(1-x_b^2\right) \\ & \left.+2\,x_WV_L\left[g_R+x_bg_L\right]+2\,x_WV_R\left[g_L+x_bg_R\right]\right\}\,, \end{aligned} \tag{2.33}$$

$$
\begin{aligned}
F_{R,L} \;=\; & \frac{1}{\Gamma}\frac{g^2|\vec{q}|}{32\pi}\left\{\left[V_L^2+V_R^2\right]\left(1-x_W^2+x_b^2\right)-4x_b\left[V_LV_R+g_Lg_R\right]\right. \\
& +\frac{m_t^2}{M_W^2}\left[g_L^2+g_R^2\right]\left(1-x_W^2-2x_b^2-x_W^2x_b^2+x_b^4\right) \\
& -2\frac{m_t}{M_W}V_L\left[g_R-x_bg_L\right]\left(1-x_b^2\right)-2\frac{m_t}{M_W}V_R\left[g_L-x_bg_R\right]\left(1-x_b^2\right) \\
& \left.+2\,x_WV_L\left[g_R+x_bg_L\right]+2\,x_WV_R\left[g_L+x_bg_R\right]\right\} \\
& \pm\frac{g^2}{64\pi}\frac{m_t^3}{M_W^2}\left\{-x_W^2\left[V_L^2-V_R^2\right]+\left[g_L^2-g_R^2\right]\left(1-x_b^2\right)+2\,x_WV_L\left[g_R+x_bg_L\right]\right. \\
& \left.-2\,x_WV_R\left[g_L+x_bg_R\right]\right\}\left(1-2x_W^2-2x_b^2-2x_b^2x_W^2+x_W^4+x_b^4\right) \qquad (2.34)
\end{aligned}
$$

where in the second equation the plus and minus sign corresponds to F_R, F_L, respectively. The following abbreviations were used: $x_W = M_W/m_t$, $x_b = m_b/m_t$ and

$$
|\vec{q}| = \frac{1}{2m_t}(m_t^4+M_W^4+m_b^4-2m_t^2M_W^2-2m_t^2m_b^2-2M_W^2m_b^2)^{1/2} \qquad (2.35)
$$

for the modulus of the W boson three-momentum in the top quark rest frame.

The dependence of F_L and F_0 with g_R is more evident than with g_L or $\mathrm{V_L}$. The g_L and V_R couplings are suppressed by the bottom quark mass, however, the interference term $V_Lg_R^*$ is not. This linear term dominates over the quadratic one, leading to a higher sensitivity of the helicity fractions to the g_R coupling. The helicity fractions are also sensitive to the phases of the anomalous couplings through the interference terms, which depend on the real part of V_R, g_L and g_R. Moreover, on the approximation of the zero b-quark mass, the lower plot in Figure 2.9 becomes symmetric around the vertical axis. The left vector-like coupling, V_L, was assumed as real and normalised to unity.

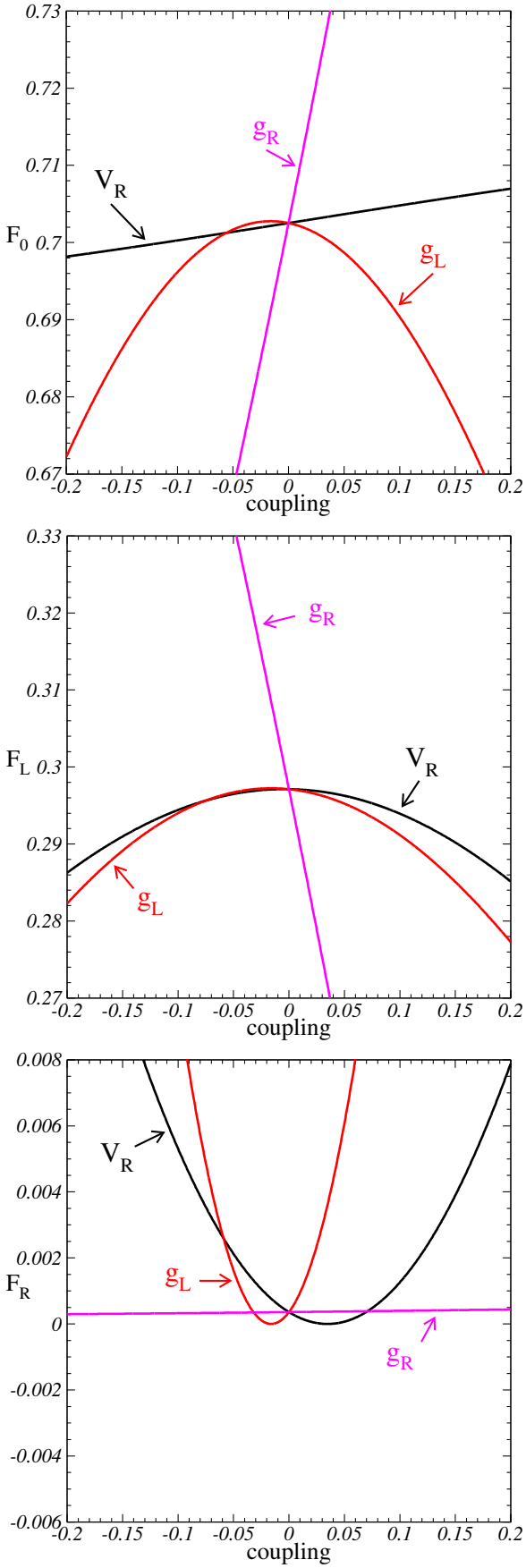

Figure 2.9: *Helicity fractions dependence on the anomalous couplings: F_0, F_L and F_R.*

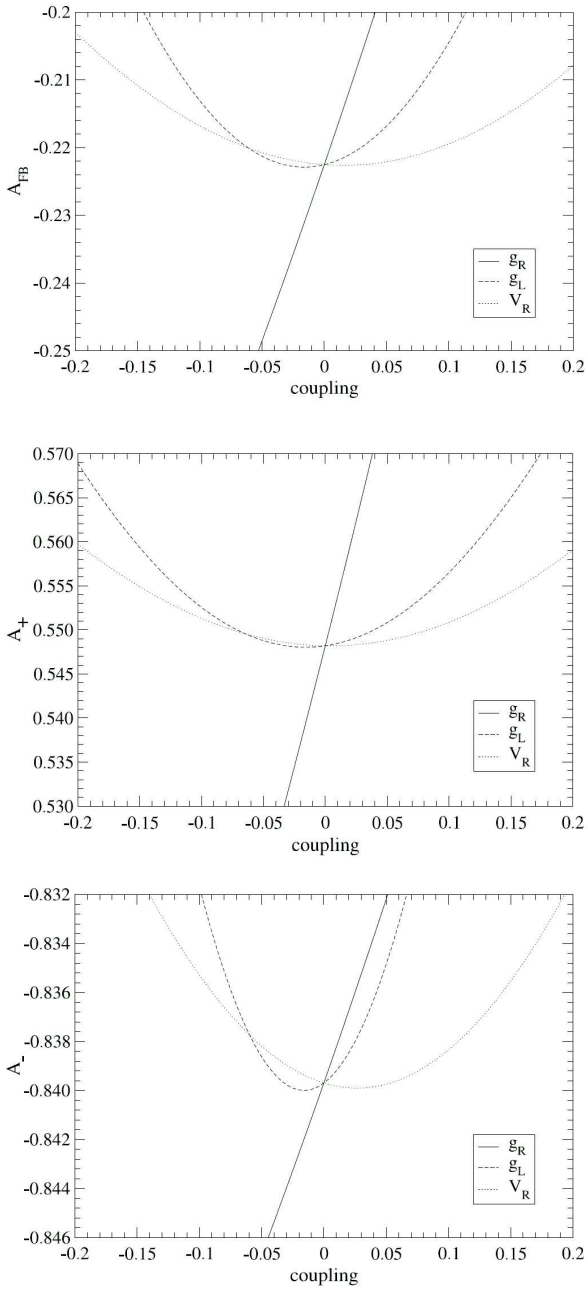

Figure 2.10: *Angular asymmetries dependence on the anomalous couplings:* A_{FB}, A_+ *and* A_-.

2.3.5 Top Quark Polarization

In the single top production, the produced t or $\bar{t}$ are highly polarized, since the weak interactions are involved. Consequently, the decay products are correlated with the top spin, as previously stated. The single top quarks are originated in a left-handed chirality state.

Additional angular asymmetries can be built from the top spin polarization. Several top decay products can be used as "spin analysers", such as $i = l^+, \nu, q, \bar{q}', W^+, b$. The angular distributions of these objects, in the top quark rest frame, is given by [25]:

$$\frac{1}{\Gamma}\frac{\mathrm{d}\Gamma}{\mathrm{d}\cos\theta_i} = \frac{1}{2}(1 + P\alpha_i \cos\theta_i) \tag{2.36}$$

where θ_i is the angle between the ith decay product momentum and the top spin direction. P is the top polarization, which is approximately 0.89 [27]. The constants α_i are called "spin analysing power" of the ith product. These constants provide information on the degree to which decay product is correlated with the top spin. In the Standard Model, and at tree level:

$$\begin{aligned} \alpha_l \quad &= \alpha_{\bar{d}} = \quad 1.00 \\ \alpha_\nu \quad &= \alpha_u = \quad -0.319 \\ \alpha_b \quad &= -\alpha_{W^+} = \quad -0.406 \end{aligned} \tag{2.37}$$

As a result, the charged lepton qualifies as the best spin analyser, since the charged lepton shows maximum correlation with the top quark spin. If CP conservation is assumed, then the distributions are the same for the antiparticles, with the exception of $\alpha_i = -\alpha_{\bar{i}}$. The Standard Model distributions at leading order are shown in Figure 2.11. The spin asymmetries are defined as [28, 29]:

$$A_i = \frac{N(\cos\theta_i > 0) - N(\cos\theta_i < 0)}{N(\cos\theta_i > 0) + N(\cos\theta_i < 0)} = \frac{1}{2}P\alpha_i \tag{2.38}$$

for each spin analyzer. In the Standard Model, the values of the spin asymmetries calculated at leading order are [29, 28]:

$$A_l = 0.445$$
$$A_\nu = -0.142$$
$$A_b = -0.181$$

In the single top production, spin asymmetries are highly sensitive to anomalous couplings, far more than in the top pair production process. Thus, the single top quark production plays a significant role in the search for new physics at the Wtb vertex.

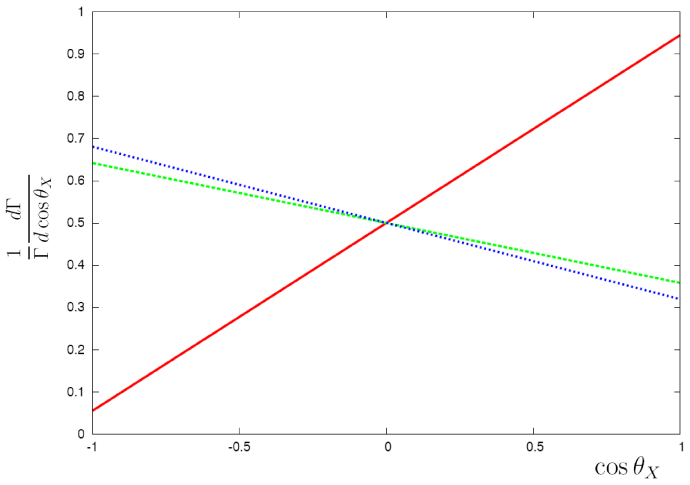

Figure 2.11: *Spin distributions of the top decay for the lepton (line), neutrino (dash), b-jet (dot), extracted from [30]*

Chapter 3

The ATLAS Experiment

The ATLAS detector is one of the main experiments at the Large Hadron Collider (LHC) at the CERN facilities. The LHC provides unprecedent conditions, allowing its experiments to perform tests of the Standard Model and search for new physics. The LHC experiments will address questions such as what gives matter its mass, what the invisible 96% of the Universe is made of, why nature prefers matter over antimatter and how matter evolved from the first instants of the Universe existence. This chapter will focus on a brief description of the CERN laboratory and the Large Hadron Collider. It will also cover the description of the ATLAS detector and its performance.

3.1 CERN

Located on the Franco-Swiss border near Geneva, the European Organization for Nuclear Research (CERN) was founded in 1954 and is run by its 20 state-members. It is one of the largest centers of scientific research of the world. Scientist from all around the world use CERN's laboratory, representing 580 universities and 85 nationalities. CERN has led to countless discoveries, both in physics and technology-related areas.

3.2 The Large Hadron Collider

The Large Hadron Collider (LHC) is a large circular particle accelerator, located at the CERN facilities, at a depth ranging from 50 to 175 m underground. It was designed to collide two beams of protons, or heavy ions, circulating in opposite directions of a 27 km ring of superconducting magnets. The accelerator tunnel was built for the previous collider, the Large Electron-Positron Collider (LEP), which collided electrons and positrons to an energy up to $\sqrt{s} = 209\,\text{GeV}$.

At LHC, the proton-proton colisons will have a center of mass energy of $\sqrt{s} = 14\,\text{TeV}$ in the next years. Or, in other words, each beam will be accelerated to a nominal energy of 7 TeV along the beam pipe. In order to obtain these high energy proton bunches, a complex injection and acceleration chain is necessary (Figure 3.1). The protons are obtained from hydrogen atoms in bunches and are injected in the linear accelerator LINAC, where they reach energies up to 50 MeV. The protons are then accelerated to 1 GeV on the Proton Sychrotron Booster (PSB) and then injected in the Super Proton Synchrontron (SPS) where they reach 450 GeV. The last step of the accelerating chain consists on the injection of two counter-rotating beams in the Large Hadron Collider, where they will reach 7 TeV. At this energy, the total cross section for proton-proton collisions will be arround 110 mb. At this energy, the 2808 bunches of particles will colide every 25 ns, with each bunch spaced by 7.55 m and taking 90 μs to complete the circular perimeter [31]. In the LHC, the design luminosity is $l = 10^{34}\,\text{cm}^{-2}\text{s}^{-1}$. This corresponds to an integrated luminosity of about $L = 100\,\text{fb}^{-1}$ per year of operation and per experiment.

Currently the LHC is already running to a energy of 3.5 TeV per beam, which corresponds to a center of mass energy of $\sqrt{s} = 7\,\text{TeV}$. During these first data taking periods, the total integrated luminosity is far from the final design luminosity. The current delivered luminosity is around $108.3\,\text{nb}^{-1}$ and the total ATLAS recorded luminosity is $\sim 97.3\,\text{nb}^{-1}$, as can be seen in Figure 3.2, last updated on 16$^{\text{th}}$ July 2010. The total integrated luminosity will suffer daily increases and by the end of the 2010 a luminosity of $100\,\text{pb}^{-1}$ is expected.

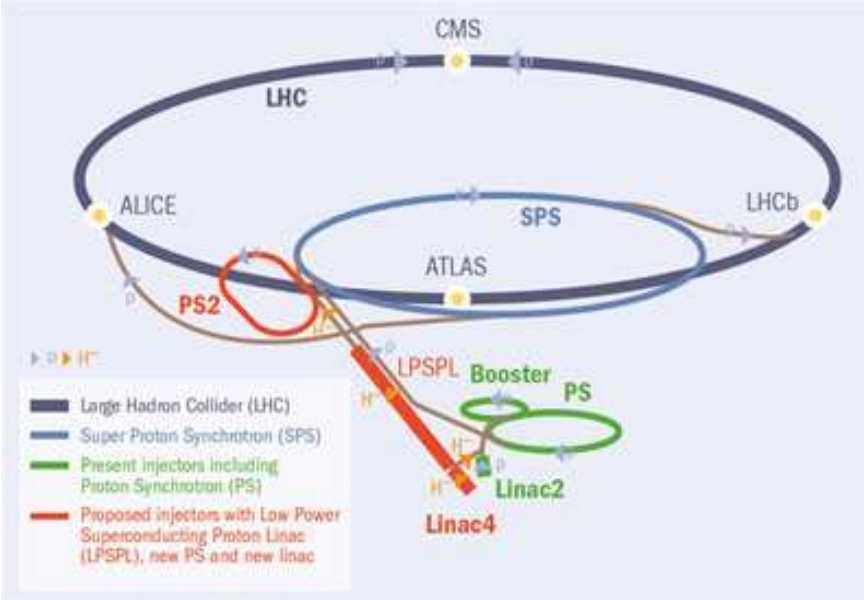

Figure 3.1: *Scheme of the injection system at LHC.*

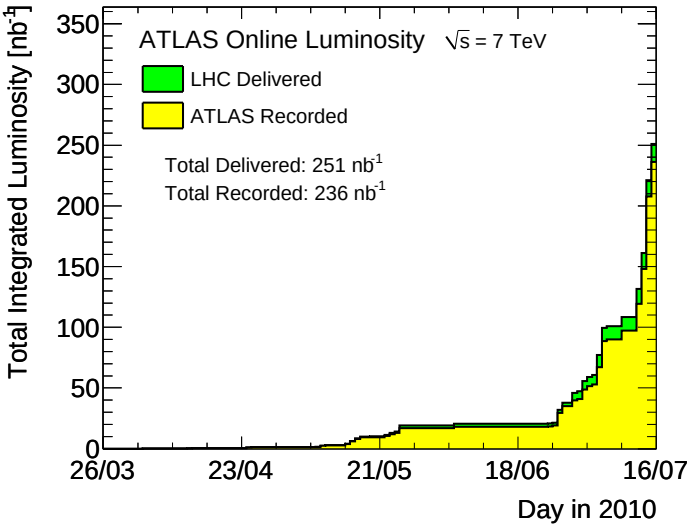

Figure 3.2: *Daily update of the total integrated luminosity at ATLAS, since the LHC startup.*

The proton beams will travel in opposite directions in separate beam pipes – two tubes kept at ultrahigh vacuum. There are several accelerating structures to boost the energy of the particles along the pipes, while the superconducting electromagnets provide a strong magnetic field to guide them around the ring. The superconducting system can be divided in 1232 superconducting main dipoles, 15 meters long, and 392 superconducting main quadropules [31]. The first are used to bend the beam, while the second ones are used to focus the beam. In order to allow the beam to flow on opposite directions, the main dipoles have two pipes, as can be seen in Figure 3.3. These dipoles producd a magnetic field of 8.33 T with electric currents of 11.85 kA, at 7 TeV [32]. For an efficient conduction, the electromagnets are built from coils of Nb-Ti (Niobium-Titanium) cable that operates in a superconducting state at temperatures under 2K. To increase the superconductor performance, the cryogenic system uses superfluid helium at 1.9 K maintaining the temperature constant. This way, the current is efficiently conducted without resistance or loss of energy. In order to keep the beams at a constant energy, superconducting radiofrequency (RF) cavities are used. At the LHC, eight RF cavities per beam, at 4.5 K, will accelerate the beam.

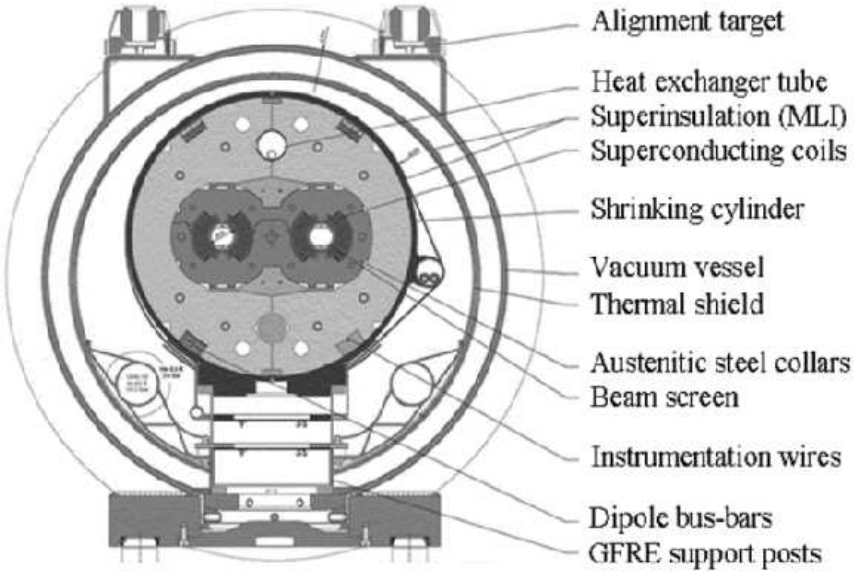

Figure 3.3: *Dipole system of the LHC, extrated from reference [32]*

The Large Hadron Collider supports six experiments: A Toroidal LHC ApparatuS (ATLAS), the LHCb, the Compact Muon Solenoid (CMS), A Large Ion Collider Experiment (ALICE), the LHCf and the TOTal Elastic and diffractive cross section Measurement (TOTEM). The first four experiments are located in large underground caverns arround the ring of the LHC, whereas the other two experiments are installed near the ATLAS detector and the CMS detector respectively. The LHC circular pipe is divided in eight octants and has four collision points, one for each main experiment, as can been seen in Figure 3.4. Some relevant LHC parameters are summarized in Table 3.1.

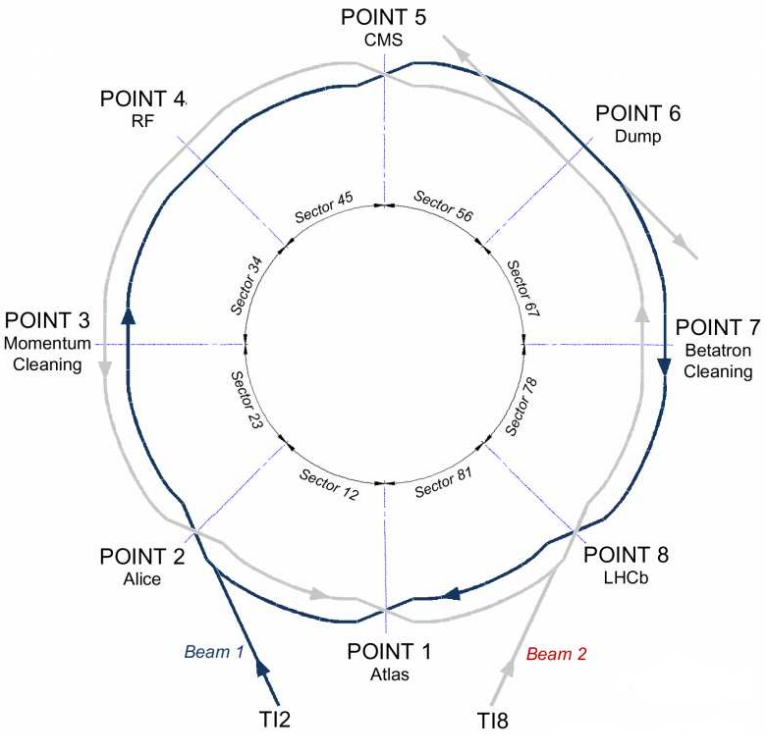

Figure 3.4: *Large Hadron Collider scheme.*

Proton energy	7 TeV
Relativistic Gamma	7461
Number of particles per bunch	1.15×10^{11}
Number of bunches	2808
Circulating beam current	0.584 A
Stored Energy per beam	362 MJ
Bunch Length	7.55 cm
Mean Bunch Length (ATLAS and CMS)	$16.7\,\mu$m
Peak Luminosity (ATLAS and CMS)	$1.0 \times 10^{34}\,\mathrm{cm}^{-2}\mathrm{s}^{-1}$

Table 3.1: *Relevant LHC beam parameters, extracted from Ref. [31] at* 14 TeV.

3.3 The ATLAS detector

The ATLAS experiment was designed to study both the standard model and the new physics processes. In order to do so, one has to identify and characterise the final state particles of the collision. For that purpose, an hermetic detector, able to measure the properties of the final state particles, was built. As most high energy physics detectors, ATLAS is a general purpose detector, constructed as a set of several cylindrical layers of subdetectors (see Figure 3.5). It is 46 m long, 25 m in diameter and weights about 7000 tonnes. In order to cover the maximum solid angle around the interation point, the cylindrical layers around the beam pipe are completed by two end-caps in the ends of the cylinder. This way, the forward-backward symmetry relative to the interation point is respected. The end-caps are also layer-shaped: several concentric discs, centred in the beam pipe. The ATLAS detector will be able to identify and measure the momentum, energy and electric charge of all stable particles produced at the interaction point, except for the neutrino[1]. For a more complete description of the ATLAS detector see Ref. [33].

Each ATLAS subdetector has a specific purpose on the particles reconstruction. The main components are, from the inside out, the inner detector, the calorimeters, the magnetic systems (toroid and solenoid magnets)

[1]The neutrino only interacts through the weak and gravitical forces, and as so, it passes through all the layers undetected.

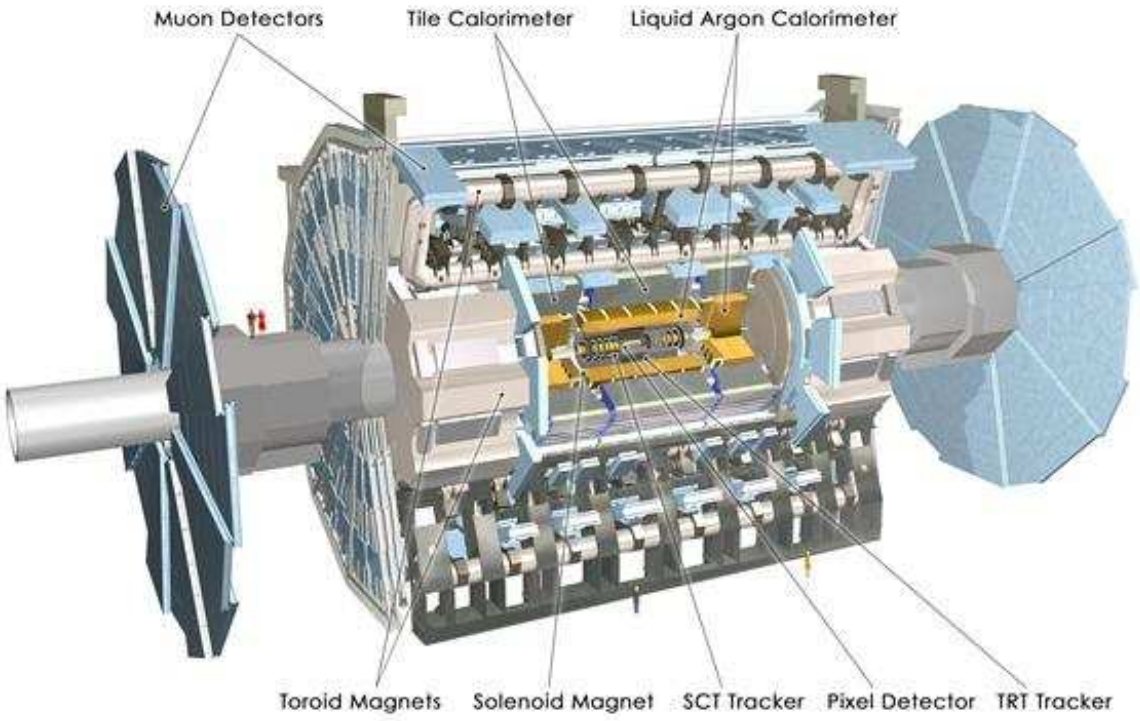

Figure 3.5: *A schematic view of the ATLAS detector.*

and the muon spectrometer. The first subdetector layer, the one nearest to the beam pipe, is the Inner Detector. It was built to record the first hits of charged particles that interact with the detector material. In order to measure the particles momenta, there is a solenoid around this detector, providing a $2\,T$ magnetic field, which curves the trajectories of very energetic particles, and hence, allows the measurement of their momentum. This is part of the magnetic system of the ATLAS detector and is called the solenoid magnet. Directly above this, is the Electromagnetic Calorimeter, which measures the energy deposited by charged particles and photons that interact via electromagnetic interation. The Hadronic Calorimeter is the next cylindrical subdetector and measures the energy of hadrons, interacting through strong interactions. The following layer is the second magnetic system of ATLAS. It is made of large toroidal magnets surrounding the calorimeters. This will provide the magnetic field for the muon spectrometer. The muon detectors are the last layer of the ATLAS detector. They are located at a radius of 4.25 m around the calorimeters and extend to the end of the detector. The momentum of the muons is computed from the defletion of their trajectories due to the magnetic field. In the following subsections, all ATLAS components will be analised in more detail.

The coordinate system used at ATLAS is a right-handed orthonormal reference system, with origin in the nominal interation-point, as can be seen in Figure 3.6. It is defined in such a way that the positive x-axis points to the center of the LHC ring, the positive y-axis points upwards and the positive z-axis is tangent to the beam pipe. The z-axis defines the detector sides. The A-side (C-side)is defined as that of positive (negative) z. The azimuthal angle, ϕ, is measured around the beam axis, so that $\phi = 0$ corresponds to the x-axis. This way it varies from $-\pi$ to π. The polar angle, θ, ranges from 0 to π and is defined as the angle between the positive z-axis and the object momentum.

Having defined the coordinate system, one can now obtain some important variables at ATLAS. For instance, the pseudorapidity is defined as:

$$\eta = -\ln(\tan(\theta/2)) \tag{3.1}$$

Since the xy plane is perpendicular to the beam pipe, it is called the trans-

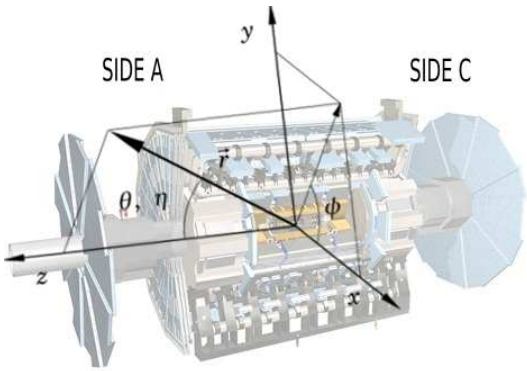

Figure 3.6: *The ATLAS coordinate system*

verse plane. Quantities such as the transverse momentum ($p_T = \sqrt{p_x^2 + p_y^2}$) and transverse energy (E_T) are measured in this plane. The distance ΔR in the pseudorapidity-azimuthal angle space is defined as $\Delta R^2 = \Delta\eta^2 + \Delta\phi^2$.

During the ATLAS design a set of requirements were taken into account, in order to enhance its preformance [34]. For instance, the detector electronics has to be fast and radiation resistant, due to the LHC experimental conditions. It should also have high granularity in order to handle the expected high particle fluxes and multiplicities and to reduce the influence of pile-up. This way the events overlap is reduced. Furthermore, a large acceptance in pseudorapidity, with very large coverage in the azimutal angle is needed. The Inner Detector is required to have good resolution in the charged particles momentum and good reconstruction efficiency. In addition, the Pixel Detectors close to the interation point have to be able to observe secondary vertices, allowing an efficient triggering and offline tagging of τ's and b-jets. It is also necessary to have electromagnetic calorimeters with large power of identification and measurement of electrons and photons, as well as hadronic calorimeters for accurate jet and missing transverse energy measurements. To determine with precision the charge of high transverse momentum (p_T) muons, an independent muon identification with good momentum resolution is needed. In order to allow the study of most physics processes of interest at LHC, ATLAS must have a triggering system for low transverse momentum

objects with sufficient background rejection. Finally, it should have forward detectors, aimed to determine the luminosity delivered at ATLAS.

The general ATLAS detector performance goals are summarised in Table 3.2.

Component	**Resolution**	η	***Trigger*** (η)
ID	$\frac{\sigma_{p_T}}{p_T} = 0.05\% p_T \oplus 1\%$	± 2.5	
EM Cal.	$\frac{\sigma_E}{E} = 10\%/\sqrt{E} \oplus 0.7\%$	± 3.2	± 2.5
Hadronic Cal.			
barrel and end-cap	$\frac{\sigma_E}{E} = 50\%/\sqrt{E} \oplus 3\%$	± 3.2	± 3.2
forward (FCal)	$\frac{\sigma_E}{E} = 100\%/\sqrt{E} \oplus 10\%$	$3.1 < \lvert\eta\rvert < 4.9$	$3.1 < \lvert\eta\rvert < 4.9$
Muon detection	$\frac{\sigma_{p_T}}{p_T} = 10\%$ at p_T=1 TeV	± 2.7	± 2.4

Table 3.2: *General detector performance, extracted from Ref. [34]. Notice that for high-p_T muons, the spectrometer performance is independent of the inner-detector system. Both E and p_T are in GeV.*

3.3.1 Inner Detector

The ATLAS tracking system is called Inner Detector (ID) and, as illustrated in Figure 3.7, it begins only a few centimeters away from the beam pipe. It extends to a radius of 1.2 m, and is 7 m long. The Inner Detector is intended to track and identify charged particles and is consists of three parts: the Pixel Detector, the Semiconductor Tracker (SCT) and the Transition Radiation Tracker (TRT). In the barrel region, they are arranged in concentric cylinders around the beam axis while at the end-cap regions they are located on disks perpendicular to the beam axis. The three sublayers are then surrounded by a solenoid magnet, which maintains the ID on a 2 T magnetic field. Due to the magnetic field, the particles are deflected, allowing the measurement of the particles momenta. The main parameters of the inner detector are summarized in Table 3.3.

The innermost part of the tracking system is the Pixel Detector, which consists of 3 cylindrical layers composed by pixel sensors and microstrips, in the central region, and 5 circular disks placed on the end-cap region. It covers

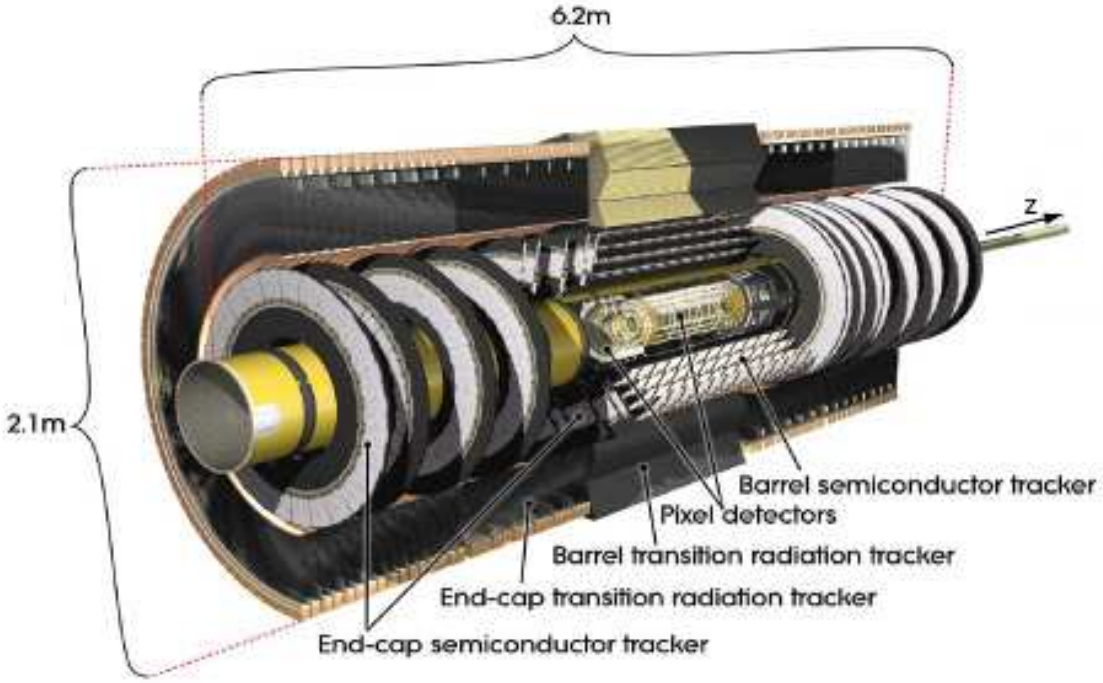

Figure 3.7: *A schematic view of the Inner Detector.*

the region $|\eta| < 2.5$. As referred, due to its location, the detectors must be very resistant to radiation. Since a large number of particles emerge from each collision, originating a high number of tracks in the tracking system, a detector with a very good granularity and momentum resolution is required. The highest granularity is achieved through the use of silicon wafers with very small pixel detectors ($R - \phi \times z = 50 \times 400\,\mu\text{m}^2$). The pixel layers are segmented in $R - \phi$ and z with typically three layers crossed by each track. The pixel detector has approximately 80.4 million read-out channels.

The Semiconductor tracker (SCT), as the name sugests, is made of semiconductor strips. It is very similar to the pixel detector, however the SCT measures particles over a larger area, which is useful for tracking in the plane perpendicular to the beam. When the charged particles cross the strips, they interact with the semicondutor, radiating electrons. These electrons are then moved to the edge of the strips (anodes), due to the presence of an electric field. The semiconductor strips are arranged in 8 layers, providing infor-

mation of four space points for each track. The SCT system is designed to provide eight precision measurements per track in the intermediate radial range, contributing to the measurement of momentum, impact parameter and vertex position. In each layer of the barrel region, there is a set of strips parallel to the beam direction. Here, the SCT has small angle (40 mrad) stereo strips, allowing the measurement of both coordinates $R - \phi$. The Semicondutor Tracker has about 6.3 million readout channels.

The Transition Radiation Tracker is the last subdetector layer of the ID. When relativistic particles cross the boundary between materials with different electrical properties, they emit radiation, which is more probable for particles with higher relativistic γ. The purpose of the TRT is to detect this radiation and thus discriminate between lighter and heavier particles, at a given energy. The structure of the TRT consists of a large number of small straw tubes (with 4 mm diameter) and a transtion radiation detector providing about 36 measurement points per track, with an accuracy of 130 μm per straw. In the barrel zone, each straw is 144 cm long, while at the end-caps 37 cm long (c.f. Figure 3.8). The total number of TRT read-out channels is about 351 thousand. The combination of the two techniques provides a very robust pattern recognition and high precision in the azimuthal angle, ϕ, and in the z coordinate. Therefore, the TRT will be able to distinguish pions from electrons by the detection of transition-radiation photons in the xenon gas mixture of the straw tubes.

The overall Inner Detector provides a full tracking coverage over $|\eta| < 2.5$, incluinding the barrel and both end-caps. The expected momentum resolution is

$$\frac{\sigma_{p_T}}{p_T} = 0.05\% \times p_T \oplus 1\% \tag{3.2}$$

3.3.2 Magnet System

The ATLAS magnetic system consists of an exceptional hybrid system of four large superconducting magnets: an inner solenoid, a barrel toroid and two end-cap toroids (Figure 3.9). The geometry of this enormous system has influenced the ATLAS structure, size, and even its name. It is intended to bend

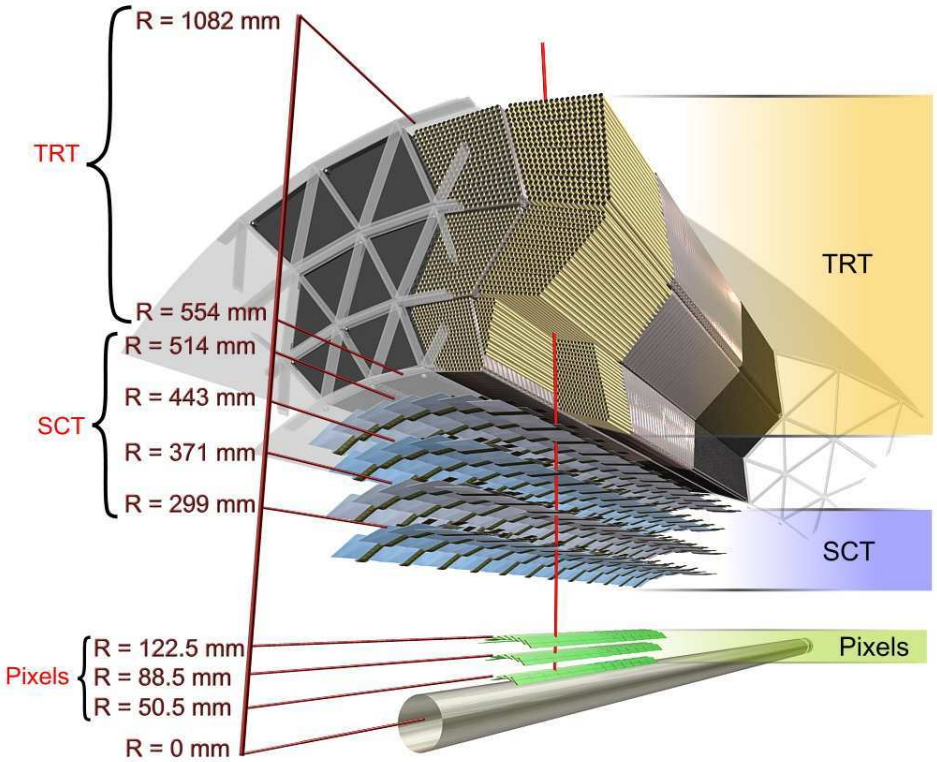

Figure 3.8: *Enlarged perspective view of the barrel zone constitution of the Inner Detector.*

the charged particles produced in each event, leading to the measurement of both their momenta and charge sign (c.f. [33]).

The inner solenoid is the closer system to the beam and provides a 2 T magnetic field parallel to the beam pipe, in the tracking system region. The solenoid is a cylindric shell, with a inner radius of 1.23 m, 10 cm thick and 5.8 m long, with a stored energy of 39 MJ. Its thickness is as low as possible so that the calorimeter can achieve the desired preformance, which resulted in a solenoid system thickness of 0.64 radiation lengths at normal incidence [36]. Due to the nearly uniform magnetic field, which is strong enough to bend even very energetic particles, the detector system will not be able to measure the momentum of low energy particles (of the order of hundreds of MeV).

System and Position	Area (m^2)	Resolution σ (μm)	Channels (10^6)	η coverage
Pixels:				
1 removable barrel layer	0.2	$R_\phi = 12$,$z = 66$	16	± 2.5
2 barrel layers	1.4	$R_\phi = 12$,$z = 66$	81	± 1.7
5 end-cap disks	0.7	$R_\phi = 12$,$z = 77$	43	$[1.7; 2.5]$
Silicon Strips:				
4 barrel layers	34.4	$R_\phi = 16$,$z = 580$	3.2	± 1.4
9 end-cap wheels	26.7	$R_\phi = 16$,$z = 580$	3.0	$[1.4; 2.5]$
TRT:				
Axial barrel straws	-	170 per straw	0.1	± 0.7
Radial end-cap straws	-	170 per straw	0.32	$[0.7; 2.5]$

Table 3.3: *Relevant parameters of the Inner Detector (extracted from Ref. [35]). Since the resolutions depend on the impact angle, the values quoted are the typical ones.*

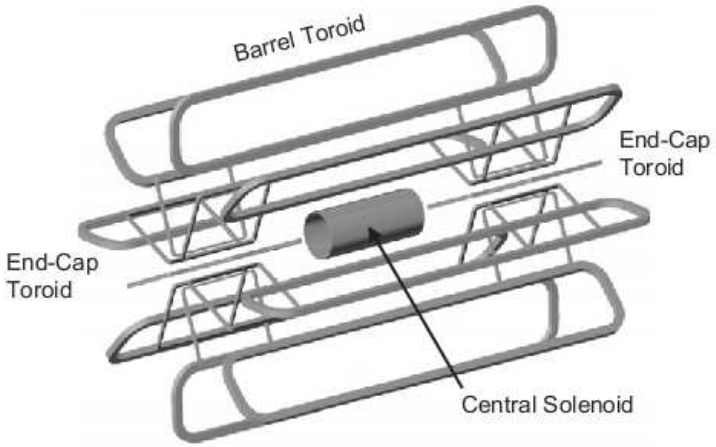

Figure 3.9: *Scheme of ATLAS magnet system (Ref. [36]).*

The barrel and end-caps toroids are composed of eight super-conducting coils, disposed radially and symmetrically around the beam pipe. The 25.3 m barrel toroid surounds the calorimeters, having an inner diameter of 9.4 m and an outer one of 20.1 m. The end-caps toroids are rotated by 22.5° in relation to the barrel toroid, leading to the overlap of the magnetic fields.

Therefore, the toroidal magnetic field in the muon spectrometer is about 0.5 T in the barrel region and about 1T in the end-caps. The barrel toroid covers the region $|\eta| < 1.0$ and the end-cap toroids cover $1.4 < |\eta| < 2.7$. In the intermediate region the magnetic field is a combination of the four magnets, and so it is not uniform.

The main parameters of the ATLAS magnet system are summarised in Table 3.4. The overall system will have a stored energy of 1.6 GJ and will operate at 4.5 K, therefore needing a special cooling system.

	Solenoid	**Barrel Toroid**	**End-Cap Toroids**
Size:			
Inner diameter	2.46 m	9.4 m	1.65 m
Outer diameter	2.63 m	20.1 m	10.7 m
Axial length	5.29 m (cold)	25.3 m	5.0 m
Number of coils	1	8	2×8
Coils:			
Turns per coil	1154	120	116
Nominal current	7.73 kA	20.5 kA	20.5 kA
Magnet stored energy	0.04 GJ	1.08 GJ	2×0.25 GJ
Peak field	2.6 T	3.9 T	4.1 T
Field range	0.9-2.0 T	0.2-2.5 T	0.2-3.5 T

Table 3.4: *Parameters of the ATLAS magnet systems (Ref. [34])*

3.3.3 Calorimeter System

The ATLAS calorimeter system consists of two different detectors for energy measurements, the electromagnetic calorimeter and the hadronic one. The electromagnetic calorimeter covers the $|\eta| < 3.2$ and serves the purpose of identifing and measuring the energy of electromagnetic-interacting particles, such as electrons and photons. On the other hand, the hadronic calorimeter was designed to identify and measure the energy of the hadrons that already crossed the electromagnetic calorimeter, covering the region of $|\eta| < 4.9$. Figure 3.10 is a cut-away view of the ATLAS calorimeter system and Table 3.5 contains the main parameters for each calorimeter, such as, the pseudorapidity coverage, granularity and segmentation in layers.

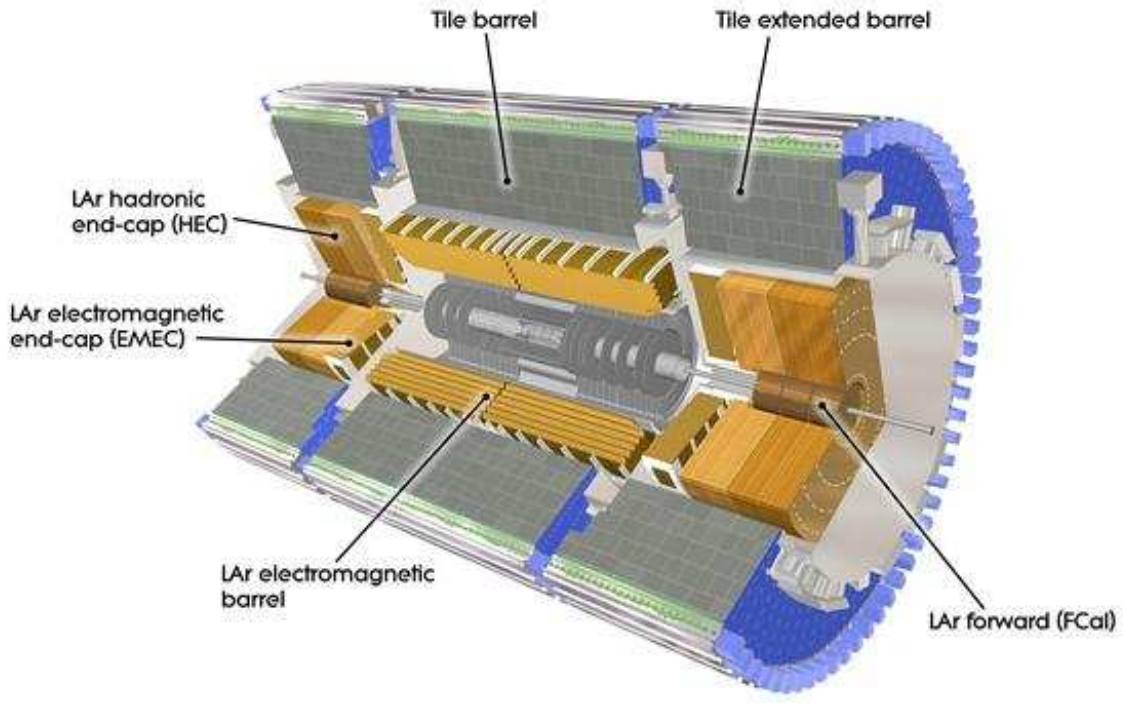

Figure 3.10: *Schematic view of the calorimeters.*

The ATLAS calorimeters not only have to contain both electromagnetic and hadronic showers, but should also guarantee that the particles reaching the muon detectors are limited to muons and undetectable neutrinos. This system is formed by several sampling detectors, maintaining azimuthal symmetry and coverage arround the beam axis. There are three cryostats that contain the calorimeters near the beam-pipe, one barrel and two end-caps, just like most sub-systems of the ATLAS detector.

The Electromagnetic Calorimeter (EM) [35] is a detector made of lead layers in an accordion geometry, with a thickness ranging between 1.1 mm and 2.2 mm. These lead layers act as passive material, while the liquid argon (LAr) distributed between them is the active material. This geometry provides full azimuthal symmetry. The lead thickness was chosen to optimize the performance in energy resolution. This calorimeter is divided into three parts: the barrel, covering the region $|\eta| < 1.475$, and two end-caps, covering

$1.375 < |\eta| < 3.2$. The central barrel is divided in two half barrels and the two end-caps are divided in two coaxial wheels at $|\eta| = 2.5$. The EM has a presampler layer, made of active LAr, located behind the cryostat wall in the pseudorapidity region of $|\eta| < 1.8$. The presampler has a thickness of 1.1 cm (0.5 cm) in the barrel (end-cap) region and is used to recover information about the energy lost by electrons and photons upstream of the calorimeter. The calorimeters preformance is then affected by the amount of material that the particles have to cross untill they reach it. For instance, at $|\eta|$ 1.5 there is a significant amount of material, corresponding to cables and service structures going to the ID. The EM has a required resolution of

$$\frac{\sigma E}{E} = \frac{10\%}{\sqrt{E}} \oplus 0.7\% \tag{3.3}$$

The hadronic calorimeter is meant to detect the particle shower that results from the quark hadronization and, after calibration, measure the energy of the original particle. It is composed by three different subdetectors: the tile calorimeter (TileCal), the LAr hadronic end-cap calorimeter (HEC) and the LAr forward calorimeter (FCal). The TileCal [34] is made of scintilator tiles (active material) intercalated by steel plates (absorving material). It covers the region $|\eta| < 1.7$ and is the first subdetector layer after the EM calorimeter, extending from an inner radius of 2.28 m to an outer radius of 4.25 m. The TileCal is divided into one barrel and two extended barrels, each with 64 modules in ϕ, covering the pseudorapidity regions of $|\eta| < 1.0$ and $0.8 < |\eta| < 1.7$, respectively. At normal incidence ($|\eta| = 0$), the radial depth of the TileCal is 9.2 interation lengths [35]. The mechanical structure of TileCal includes the electronic and read-out systems, in order to collect the light produce in the scintillating tiles. The light is collected at the edges of each tile, using wavelength shifting optical fibres, connected to photomultiplier tubes. The HEC is a sampling calorimeter made of copper plates and LAr layers of active medium. It covers the region $1.5 < |\eta| < 3.2$ overlapping the forward calorimeter. The HEC is a two wheel system with an inner radius of 0.475 m and an outer one of 2.03 m. Each wheel is divided in two longitudinal segments and has 32 modules in ϕ. It shares each of the two LAr end-cap cryostats with the EM end-cap and FCal. Finally, the last

hadronic subdetector is the FCal, located in each of the ATLAS end-caps. The FCal are divided into three modules according to the different passive materials used. The first module uses copper as passive medium, while the other two use tungsten. In all three modules the active medium is LAr. The FCal is located at 4.5 m from the interacting point, and cover the region $3.1 < |\eta| < 4.9$. It has the main purpose of minimizing the loss of energy and reduce background radiation levels in the muon spectrometer. The total radiation length of this calorimeter is about 10λ and has a required resolution of

$$\frac{\sigma_E}{E} = \frac{50\%}{\sqrt{E}} \oplus 3\% \tag{3.4}$$

on the barrel region and

$$\frac{\sigma_E}{E} = \frac{100\%}{\sqrt{E}} \oplus 10\% \tag{3.5}$$

in the end-caps.

The energy distribution of the TileCal cells from collision data at 7 TeV, 2.36 TeV, and 0.9 TeV can be seen in Figure 3.11 together with randomly triggered events and Monte Carlo simulation at 7 TeV. Each distribution is normalized by the number of events. The achieved agreement between data and Monte Carlo is remarkable and suggests a very good comprehension of the detector.

3.3.4 Muon System

The muon spectrometer is the last set of ATLAS subdetectors and is based on the magnetic deflection of muon tracks [34]. Since particles have to cross the rest of the systems before getting to the spectrometer, muons are the only charged particles expected to reach it. This detector extends from a 4.25 m radius around the calorimeters to the outer radius of the detector. The muon system has different configurations according to the region of the detector. In the barrel it consists of cylindrically arranged chambers, while in the end-caps, the chambers are disposed vertically (c.f. Figure 3.12).

The muon spectrometer works under the same principle of the inner detector, since muons curve in the magnetic field, allowing the measurement

	Barrel		End-Cap	
EM calorimeters				
$\|\eta\|$ coverage:				
presampler	(1 layer)	$\|\eta\| < 1.52$	(1 layer)	$1.5 < \|\eta\| < 1.8$
calorimeter	(3 layers)	$\|\eta\| < 1.35$	(2 layers)	$1.375 < \|\eta\| < 1.5$
	(2 layers)	$1.35 < \|\eta\| < 1.475$	(3 layer)	$1.5 < \|\eta\| < 2.5$
			(2 layer)	$2.5 < \|\eta\| < 3.2$
Granularity ($\Delta\|\eta\| \times \Delta\phi$ vs $\|\eta\|$):				
presampler	0.025×0.1	$\|\eta\| < 1.52$	0.025×0.1	$1.5 < \|\eta\| < 1.8$
calorimeter 1st layer	$0.025/8 \times 0.1$	$\|\eta\| < 1.4$	0.050×0.1	$1.375 < \|\eta\| < 1.425$
	0.025×0.025	$1.4 < \|\eta\| < 1.475$	0.025×0.1	$1.425 < \|\eta\| < 1.5$
			$0.025/8 \times 0.1$	$1.5 < \|\eta\| < 1.8$
			$0.025/6 \times 0.1$	$1.8 < \|\eta\| < 2.0$
			$0.025/4 \times 0.1$	$2.0 < \|\eta\| < 2.4$
			0.025×0.1	$2.4 < \|\eta\| < 2.5$
			0.1×0.1	$2.5 < \|\eta\| < 3.2$
calorimeter 2nd layer	0.025×0.025	$\|\eta\| < 1.4$	0.050×0.025	$1.375 < \|\eta\| < 1.425$
	0.075×0.025	$1.4 < \|\eta\| < 1.475$	0.025×0.025	$1.425 < \|\eta\| < 2.5$
			0.1×0.1	$2.5 < \|\eta\| < 3.2$
calorimeter 3rd layer	0.050×0.025	$\|\eta\| < 1.35$	0.050×0.025	$1.5 < \|\eta\| < 2.5$
Readout Channels:				
presampler		7808		1536 (both sides)
calorimeter		101760		62208 (both sides)
Scintillator TileCal				
$\|\eta\|$ coverage:	(3 layers)	$\|\eta\| < 1.0$	(3 layers)	$0.8 < \|\eta\| < 1.7$
Granularity ($\Delta\|\eta\| \times \Delta\phi$):		0.1×0.1		0.1×0.1
	(last layer)	0.2×0.1	(last layer)	0.2×0.1
Readout Channels:		5760		4092 (both sides)
LAr Hadronic End-Cap				
$\|\eta\|$ coverage:			(4 layers)	$1.5 < \|\eta\| < 3.2$
Granularity ($\Delta\|\eta\| \times \Delta\phi$):			0.1×0.1	$1.5 < \|\eta\| < 2.5$
			0.2×0.2	$2.5 < \|\eta\| < 3.2$
Readout Channels:				5632 (both sides)
LAr Forward Calorimeter				
$\|\eta\|$ coverage:			(3 layers)	$3.1 < \|\eta\| < 4.9$
Granularity ($\Delta\|\eta\| \times \Delta\phi$):			FCal 1	3.0×2.6
			FCal 2	2.3×4.2
			FCal 3	5.4×4.7
Readout Channels:				3524 (both sides)

Table 3.5: *Important parameters of each of the ATLAS Calorimeters (Ref. [34]).*

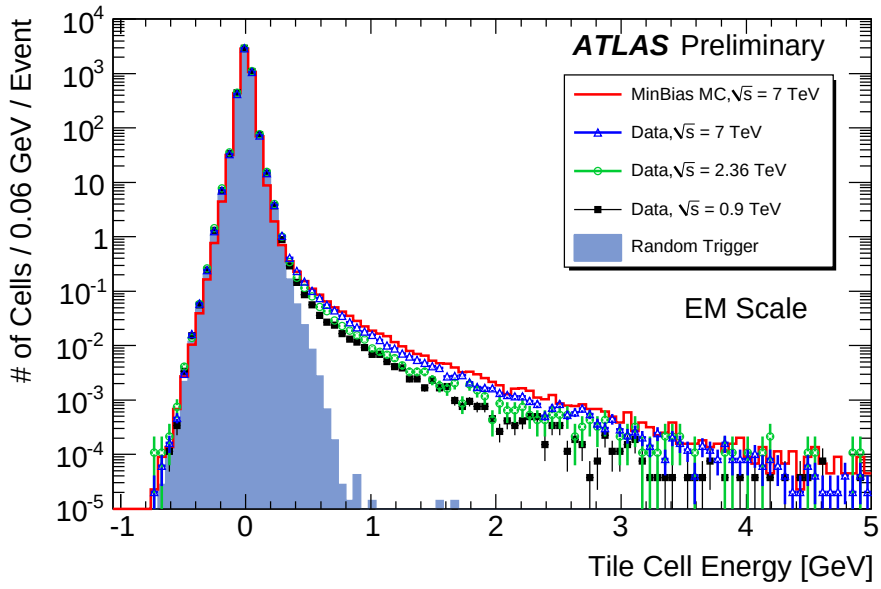

Figure 3.11: *Energy deposition on the TileCal cells for* 7 TeV*,* 2.36 TeV*, and* 0.9 TeV *collision data superimposed with Pythia minimum bias Monte Carlo and randomly triggered events.*

of their momentum and charge sign. The muon trajectories curve due to the magnetic field of the barrel toroid in the $|\eta| < 1.4$ region and in the $1.6 < |\eta| < 2.7$ regions due to the end-cap toroids. The magnetic field in the region defined by $1.4 < |\eta| < 1.6$ is a combination of the fields produced by both toroids. This system has full coverage in the pseudorapidity $|\eta| < 2.7$, except around $|\eta| = 0$, where there is a 300 mm hole, allowing the passage of the services for the ID detector, inner solenoid and calorimeters, which will significantly degrade the muon reconstruction in that area. There are three subdetectors both in the barrel and in the end-caps. The measurement of the track coordinates is made by the Monitored Drift Tubes (MDT). These consist in aluminium-walled gaseous drift chambers, under a high electric field, where the passing muons ionize the gas. For pseudorapidities between 2.0 and 2.7, the Cathode Strip Chambers (CSC) are used. These consist in multiwire proportional chambers with cathodes segmented into strips and high granularity, as required in this region. The Resistive Plate Chambers (RPC)

(in the barrel zone) and the Thin Gap Chambers (TGC) (in the end-caps) cover the region $|\eta| < 2.4$, as part of the trigger system. The relevant parameters of the muon system are shown in Table 3.6. The muon spectrometer has a resolution of $\sigma_{p_T}/p_T = 10\%$ at $p_T = 1$ TeV.

3.3.5 Trigger and data acquisition system

The LHC will have bunches of particles crossing every 25 ns, at a 40 MHz rate. At nominal luminosity, there will occur approximately 20 collisions per bunch. Therefore, at ATLAS there will be a rate of 10^9 interations per second, originating 1 petabyte/second of raw data. Due to electronic delay, the detector can only respond in 2.5 μs, leading to a rate of ~ 200 Hz storage capability [37]. In order to reduce the incoming interation rate from about 1 GHz to $\sim$ 200 Hz and select the interesting hard-scattered interations, a trigger system was installed. The trigger and data acquisition systems (DAQ)

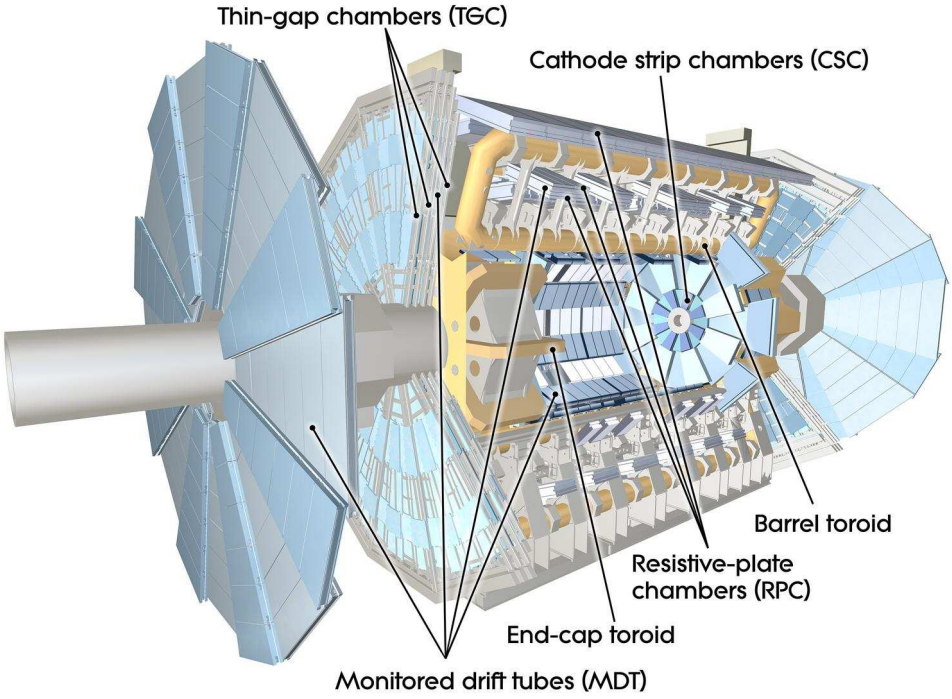

Figure 3.12: *Overview of the muon chambers.*

Monitored Drift Tubes (MDT)	
Coverage	$\|\eta\| < 2.7$ (innermost layer: $\|\eta\| < 2.0$)
Number of Chambers	1150
Number of Channels	354000
Function	Precision Tracking
Cathode Strip Chambers (CSC)	
Coverage	$2.0 < \|\eta\| < 2.7$
Number of Chambers	32
Number of Channels	31000
Function	Precision Tracking
Resestive Plate Chambers (RPC)	
Coverage	$\|\eta\| < 1.05$
Number of Chambers	606
Number of Channels	373000
Function	Triggering, Second Coordinate
Thin Gap Chambers (TGC)	
Coverage	$1.05 < \|\eta\| < 2.7$ (for triggering: $\|\eta\| < 2.4$)
Number of Chambers	3588
Number of Channels	318000
Function	Triggering, Second Coordinate

Table 3.6: *Main parameters of the ATLAS Muon Spectrometer for the final configuration of the detector in 2009 (Ref. [34])*

are based on signatures of particles with high p_T and missing transverse energy, and are divided in three levels of event selection (Figure 3.13): L1, L2 and the Event Filter.

The first level of trigger (L1) selects high p_T muons, electrons, photons, jets and τ leptons decaying in hadrons. The decision is made using the measured E_T values in trigger towers of 0.1×0.1 granularity in $\Delta\eta \times \Delta\phi$. Therefore, based on the reduced-granularity information from a subset of fast detectors, the L1 trigger takes about 2 μs to make a decision (including the signal transmission betweeen detector and trigger electronics). During the information exchange period, all of the data is kept in the pipeline memory. Afterwards, the selected events are transferred to the Readout Buffers (ROBs), via the Readout Drivers (RODs). When data is formatted and stored in ROB, the event rate is about 75 kHz.

For each selected event, L1 also provides regions in η and ϕ where its selection process has identified interesting features, which are called Regions of Interest (RoI). The RoIs also register the criteria passed by the event. The data will now be analysed by the L2 trigger and the Event Filter, which constitute the High Level Trigger (HLT). The L2 uses RoI information in coordinates, energy and topologies, to chose which data to be readout from the detector. Since the L2 trigger analyses the RoIs sent by L1, it will only access to about 2% of the total event data in order to take its decision. After this trigger level, which has a latency of 1 s, the event rate is around 3 kHz.

The data is then transferred to the EF, through the Sub-Farm Input (SFI). After fully reconstructed by the EF (through off-line procedures), the events undergo a final selection. This trigger has a latency of $\sim$ 4 s and achieves an event rate of about 200 Hz, as required. The selected events will then go to the Sub-Farm Output (SFO) and will be stored to be analysed off-line.

The trigger requirements are labeled with a code made out of a combination of letters and numbers. The letters indicate the type of object being triggered: whether it is an electromagnetic clusters (EM), electrons (e) or muons (MU or mu). The capital letters indicate that they are triggered in the L1 and the lower-case letters indicate the HLT. The numbers right after these letters represent the transverse momentum of the object for which the trigger is 95% efficient. If the letter i or I is in the code, then an isolation criteria was applied. For example, "2e15i" means that there is a 95% efficiency for triggering an event with two isolated electrons with a p_T higher than 15 GeV.

3.4 GRID

The ATLAS experiment will be collecting and storing about 15 Petabytes (15 million Gigabytes) of data annually produced by the LHC. This vast amount of data requires the use of large storage and computing resources. In order to have global data access, a worldwide Grid computing system was developed for the LHC experiments [38].

The LHC data will be distributed in organized Tiers (four-tiered model).

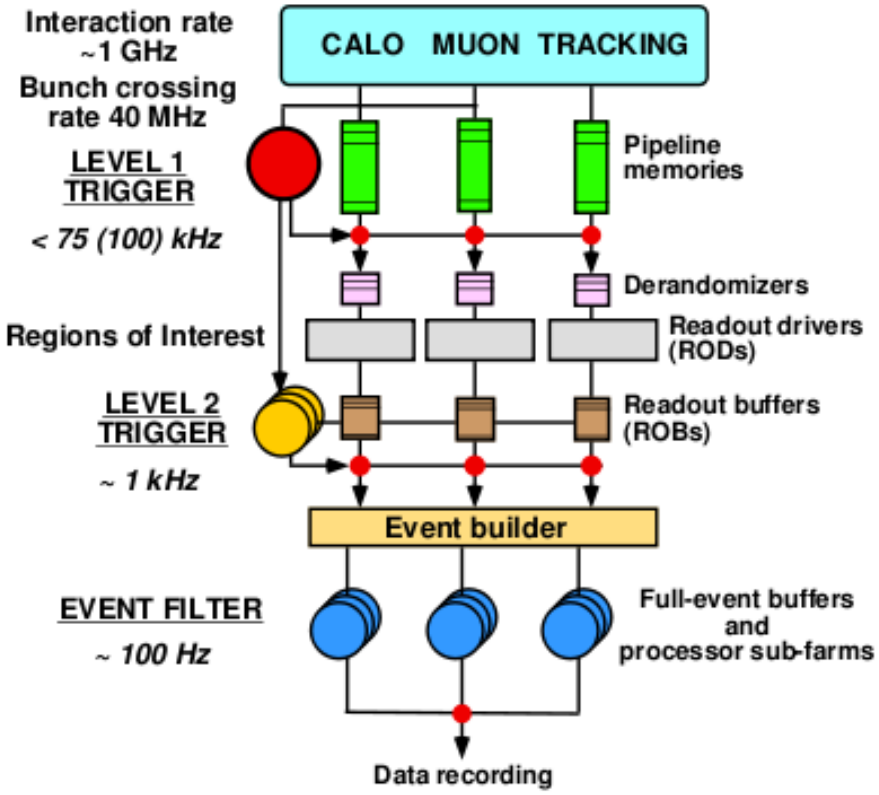

Figure 3.13: *Block Diagram of the Trigger and DAQ system (extracted from Ref. [35]).*

The first tier, Tier-0, is located at CERN where the data is produced. This tier has a primary backup recorded on tape and is connected to eleven Tier-1 sites through high-speed networks (10 Gb/s). These Tier-1 sites, located in different countries, will store the output of event reconstruction and make the data available to more than 150 Tier-2 centers. Each Tier-2 consists of collaborating computing facilities, able to store enough data and provide adequate computing power for specific analysis tasks. The last part of the Grid system is the Tier-3, which consist of local computing clusters, from where individual scientists will access the data.

Chapter 4

Generation and Simulation of Events

In order to study the processes involved in proton-proton collisions, the use of large samples of simulated events is required. In this chapter the generation of these events, based on Monte Carlo (MC) techniques is described. The interactions of each resulting particle with the ATLAS detector were simulated using GEANT4 [39], including detector details, allowing a realistic study of the performances of particle reconstruction and trigger.

4.1 Signal and Background Processes

In the present analysis, the single top s-channel process ($t \rightarrow W^+b$), where the W boson decays leptonically $W \rightarrow l\nu_l$, is considered as signal (with $l = e^{\pm}$, $\mu^{\pm}$, $\tau_l^{\pm}$). The hadronic τ decays are considered as background to this signal. Since there are two b quarks in the final topology, the one coming directly from the top quark will be named as "leptonic b" and the one coming from the virtual boson will be named "recoil b", as it is expected to have a trajetory with opposite direction to the top quark trajectory. The background channels are the other SM processes that can fake the s-channel topology, such as the other single top channels (t-channel and Wt associate production), $t\bar{t}$, W+jets, Z+jets, WW , ZZ , WZ and QCD.

In proton-proton collisions, the protons are treated as composed by a set

of partons, the quarks and the gluons, which are described by structure functions. The Parton Distribution Functions (PDF) describe the distribution of the momentum fraction (x) of the partons in a proton, as a function of the squared momentum transfer, Q^2 , carried by the exchanged particle in the scattering. In order to calculate the production cross sections, the knowledge of the PDF's is essential, since it provides the partonic structure of hadrons. Due to the inherent non-perturbative effect in a QCD binding state, the PDF cannot be calculated perturbatively, instead they are obtained using experimental data.

According to the SM, quarks and gluons cannot manifest themselves as free particles, due to confinement of the strong force. Thus, they form colour-neutral hadrons. As a result, the quarks and gluons produced in the interaction are detected as jets of hadrons. This process is called hadronization and its explicit calculation has not yet been perfomed due to its non-perturbative nature [40]. In order to simulate the hadronization mechanism, Monte Carlo methods based on phenomenological models are used. For instance, the MC@NLO and ALPGEN Monte Carlo generators implement different hadronization models with next-to-leading order (NLO) and leading order (LO) accuracy, respectively. In the MC samples used in this thesis, the parton showering was performed by HERWIG [41].

The ATLAS detector simulation is used so that the detector effects are taken into account. The detector simulation can be done either using a fast simulation or the full GEANT4 simulation. The first one, as the name suggests, is faster and allows the simulation of very large samples of signal and background events, by parameterizing the expected performance of the detector. The full simulation (FullSim), although much more demanding from the computational point of view, takes into account the detector interaction details, allowing a more realistic study of the performances of particle reconstruction and trigger. In the current study, the FullSim is used.

4.2 Monte Carlo Generation

In this thesis, the utilized MC samples are the ATLAS mc09 generated at a center-of-mass energy of 7 TeV. These were reconstructed with version

15.6.7.8.1 of the ATLAS software Athena [42], and formatted into D3PDs using the package TopPhysD2PDMaker-00-02-21.

The single top and $t\bar{t}$ processes were generated using version 3.41 of the MC@NLO generator [43]. This MC generator produces final states at NLO accuracy, which are then passed to the Herwig parton shower MC with leading-logarithmic (LL) accuracy. All events were generated assuming the top mass $m_t = 172.5\,\text{GeV}$ (with a width 1.320 GeV [20]) and the W boson mass $m_W = 80.403\,\text{GeV}$, with a width 2.141 GeV.

In the $t\bar{t}$ pair production samples spin correlations are implemented. The samples are normalised to reproduce the cross section calculated at NLO + next-to-next-to-leading-logarithmic (NNLL) precision. Since these samples have event weight of +1 or -1, only the sum of the weights is a physical quantity. In this scheme the total cross section is 80.20 pb at a centre-of-mass energy of 7 TeV. The kinematic distributions have a relatively constant shape, but the overall normalization must be fixed to a realistic value, since the $\sigma_{\text{NLO}}/\sigma_{\text{LO}}$ ratio ("k-factor") is rather large for $t\bar{t}$ production. To normalize the samples to the approximate NNLO cross section, it suffices multipling by the k-factor. Table 4.1 presents the matrix element generator, parton shower, cross sections, k-factors, number of events and luminosity of the samples.

The single top baseline samples include all the three channels: s-, t- and Wt-channel. However, two different schemes are used: for the MC@NLO samples requested the diagram-removal scheme has been used for Wt production, but it is envisaged that a separate set will be produced with the diagram subtraction scheme as a cross check. The samples are summarised in Table 4.1 (note that no k-factor is needed).

The other relevant processes for this study, $W + b\bar{b}$, $W + jets$, $Z + jets$, WW, ZZ, WZ and QCD multijet events, do not directly involve top quarks. Nevertheless, their final state topology can lead to a mis-identification of a top quark. Therefore, together with the $t\bar{t}$ process, these constitute the background for the s-channel single top analysis. With the exception of the $t\bar{t}$ process, these processes were generated with the ALPGEN generator version 2.13 [44], which is a LO generator, containing the matrix elements for $2 \to n$ processes. Thus, the generation of multijet final states is more accurate than with a LO generator for $2 \to 1$ and $2 \to 2$ process together

with LL parton shower algorithms.

Background events coming from the $W + n$ jets (n = 0,...,5) processes were generated with ALPGEN interfaced with HERWIG. The W+jets samples include hard jets from the matrix element arising from gluons, or light quarks (u, d, s and c quarks, all treated as massless). In these samples, the parton shower may also produce b quarks, which will have predominantly low transverse momentum (less than 15 GeV). The details of the samples are summarised in Table 4.1.

As the current analysis is dependent on the b quark tagging tool, the $W+b\bar{b}$ production is an important background. The considered samples were generated using ALPGEN and only include b jets produced via the matrix element. These samples have a small ($\sim 4\%$) overlap with the b production in the W+jets [43]. The overlap was reduced by chosing phase space cuts in the generation of the samples. Therefore, the use of these samples with the W+jets ones is not double counting events.

The Z+jets samples were generated using two different processes: the Z+light and the Z+heavy-quark jets similarly to the W jets samples. These samples do not contain Z events exclusively: the full Drell-Yan contribution from the process $\gamma* \rightarrow ll$ are included. Moreover, the $Z/\gamma*$ interference is taken into account. Since the dileptons were generated in the invariant mass (M_{ll}) range of 40 GeV $<$ M$_{\rm ll}$ $<$ 2000 GeV, the cross sections refered in Table 4.1 are the total Drell-Yan cross sections in that invariant mass range.

The diboson (WW, ZZ and WZ) events were generated with ALPGEN. For these events a filter requiring a generated electron or a muon with $p_T >$ 10 GeV was applied. In the WW samples, only events with both W bosons decaying leptonically were simulated. In the case of the WZ samples, events were produced with inclusive W decays and $Z \rightarrow ll$. The ZZ samples were generated considering one $Z \rightarrow ll$ and the other fully inclusive.

Finally, the simulation of QCD multijet events was also done with ALPGEN. Like the W+jets, the generation of the heavy flavour and light jet events was done separately. Since the multijet production has a large cross section, in order to have sufficient statistics for the top quark analyses two strategies were applied in the generation process:

- **Transverse momentum (p_T) slicing:** The QCD multijet events were

generated in slices of transverse momentum, since the cross section falls rapidly with increasing jet transverse momentum, ensuring the sufficient high P_T statistics without generating too many low P_T events. The samples were named according to the p_T slice : JX refers to p_T slicing with J3 at higher p_T than J2, and so on.

- **Filtering:** The generation was done using two filters: a jet and a μ filter. In the jet filtered samples the events are required to contain at least three jets with $p_T > 25\,\text{GeV}$ and a fourth jet with $p_T > 17\,\text{GeV}$. The jets are generated using the Anti-kT algorithm [45]. The muon filtered samples were simply required to contain at least one muon with a $P_T > 10\,\text{GeV}$, using the mu10 filter. The filtered samples are not required to be orthogonal, thus some overlap is possible to occur.

In this study, only the sliced and the μ filtered samples were used. The details of the used samples can be seen in Table 4.2.

In order to have a good simulation of the data, it is desirable to have the most accurate expectation of the background MC possible. The normalization of the utilized MC samples was done through the use of k-factors, however, in the future, many of the backgrounds should also be normalised via data-driven methods. The use of such methods is beyond the scope of this thesis.

4.3 Simulation of events

The GEANT4 was used to fully simulate the interactions of the partons with the ATLAS detector [39]. In the simulation of the ATLAS detector misalignemts of the LAr calorimeters and muon system were included. The LAr and inner detector were considered to have distorted materials and the magnetic field initial displacement is also included.

The FullSim simulates the deposition of energy of all stable particles for each event in the calorimeters cells. Thus the D3PD's include a list of reconstructed jets, leptons and missing transverse energy. The region inside a $\Delta R = 0.4$[1] cone defines a group of calorimeter cells and only groups with

[1] $\Delta R = \sqrt{\Delta\eta^2 + \Delta\Phi^2}$

Process	Generator	Parton Shower	σ (pb)	K-factor	N_{events}	Lum. (fb^{-1})
singletop s-channel ($e\nu$)	MC@NLO	Herwig	0.4685	1	9950	21.23800
singletop s-channel ($\mu\nu$)	MC@NLO	Herwig	0.4684	1	9996	21.23800
singletop s-channel ($\tau\nu$)	MC@NLO	Herwig	0.4700	1	9996	21.26808
singletop t-channel ($e\nu$)	MC@NLO	Herwig	7.152	1	9993	1.39724
singletop t-channel ($\mu\nu$)	MC@NLO	Herwig	7.176	1	9997	1.39312
singletop t-channel ($\tau\nu$)	MC@NLO	Herwig	7.128	1	10000	1.40292
singletop Wt production	MC@NLO	Herwig	14.581	1	14995	1.0284
$t\bar{t}$ no full hadronic decays	MC@NLO	Herwig/Jimmy	80.201	1.09	139917	1.60054
$W \to e\nu + 0$jets	ALPGEN	Herwig/Jimmy	6913.3	1.22	1381931	0.16384
$W \to e\nu + 1$jets	ALPGEN	Herwig/Jimmy	1293.0	1.22	258408	0.16382
$W \to e\nu + 2$jets	ALPGEN	Herwig/Jimmy	377.1	1.22	188896	0.41058
$W \to e\nu + 3$jets	ALPGEN	Herwig/Jimmy	100.9	1.22	50477	0.41006
$W \to e\nu + 4$jets	ALPGEN	Herwig/Jimmy	25.3	1.22	12991	0.42080
$W \to e\nu + 5$jets	ALPGEN	Herwig/Jimmy	6.9	1.22	3449	0.40972
$W \to \mu\nu + 0$jets	ALPGEN	Herwig/Jimmy	6935.4	1.22	1346046	0.15908
$W \to \mu\nu + 1$jets	ALPGEN	Herwig/Jimmy	1281.2	1.22	255909	0.16372
$W \to \mu\nu + 2$jets	ALPGEN	Herwig/Jimmy	375.3	1.22	187860	0.41030
$W \to \mu\nu + 4$jets	ALPGEN	Herwig/Jimmy	25.7	1.22	12991	0.41434
$W \to \mu\nu + 5$jets	ALPGEN	Herwig/Jimmy	7.0	1.22	3498	0.40960
$W \to \tau\nu + 0$jets	ALPGEN	Herwig/Jimmy	6835.8	1.22	1365491	0.16374
$W \to \tau\nu + 1$jets	ALPGEN	Herwig/Jimmy	1276.8	1.22	254753	0.16354
$W \to \tau\nu + 2$jets	ALPGEN	Herwig/Jimmy	376.6	1.22	188446	0.41016
$W \to \tau\nu + 3$jets	ALPGEN	Herwig/Jimmy	100.8	1.22	50472	0.41042
$W \to \tau\nu + 4$jets	ALPGEN	Herwig/Jimmy	25.7	1.22	12996	0.41450
$W \to \tau\nu + 5$jets	ALPGEN	Herwig/Jimmy	7.0	1.22	3998	0.46814
$Wb\bar{b} + 0$jets	ALPGEN	Herwig/Jimmy	3.2	1.22	6499	1.66470
$Wb\bar{b} + 1$jets	ALPGEN	Herwig/Jimmy	2.6	1.22	5500	1.73392
$Wb\bar{b} + 2$jets	ALPGEN	Herwig/Jimmy	1.4	1.22	2997	1.75468
$Wb\bar{b} + 3$jets	ALPGEN	Herwig/Jimmy	0.6	1.22	1500	2.04918
$Z \to ee + 1$jets	ALPGEN	Herwig/Jimmy	661.9	1.22	304216	0.37672
$Z \to ee + 2$jets	ALPGEN	Herwig/Jimmy	133.3	1.22	63440	0.39010
$Z \to ee + 3$jets	ALPGEN	Herwig/Jimmy	40.3	1.22	19497	0.39656
$Z \to ee + 4$jets	ALPGEN	Herwig/Jimmy	11.2	1.22	5499	0.40244
$Z \to ee + 5$jets	ALPGEN	Herwig/Jimmy	2.7	1.22	1499	0.45506
$Z \to ee + 6$jets	ALPGEN	Herwig/Jimmy	0.8	1.22	500	0.51230
$Z \to \mu\mu + 0$jets	ALPGEN	Herwig/Jimmy	657.7	1.22	303947	0.37880
$Z \to \mu\mu + 1$jets	ALPGEN	Herwig/Jimmy	132.8	1.22	62996	0.38882
$Z \to \mu\mu + 2$jets	ALPGEN	Herwig/Jimmy	39.6	1.22	18993	0.39314
$Z \to \mu\mu + 3$jets	ALPGEN	Herwig/Jimmy	11.1	1.22	5497	0.40592
$Z \to \mu\mu + 4$jets	ALPGEN	Herwig/Jimmy	2.8	1.22	1499	0.43882
$Z \to \mu\mu + 5$jets	ALPGEN	Herwig/Jimmy	0.8	1.22	499	0.51128
$Z \to \tau\tau + 0$jets	ALPGEN	Herwig/Jimmy	657.4	1.22	303359	0.37824
$Z \to \tau\tau + 1$jets	ALPGEN	Herwig/Jimmy	133.0	1.22	63481	0.39098
$Z \to \tau\tau + 2$jets	ALPGEN	Herwig/Jimmy	40.4	1.22	19492	0.39548
$Z \to \tau\tau + 3$jets	ALPGEN	Herwig/Jimmy	11.0	1.22	5497	0.40902
$Z \to \tau\tau + 4$jets	ALPGEN	Herwig/Jimmy	2.9	1.22	1499	0.42368
$Z \to \tau\tau + 5$jets	ALPGEN	Herwig/Jimmy	0.7	1.22	499	0.58430
WW Pairs	ALPGEN	Herwig	11.75	-	249837	21.26260
WZ Pairs	ALPGEN	Herwig	3.432	-	249725	255.34854
ZZ Pairs	ALPGEN	Herwig	0.977	-	249830	72.79428

Table 4.1: *For each process, the MC generator, parton shower used, cross section, k-factor, number of generated events and respective luminosity is shown.*

Process	Generator	Parton Shower	σ (pb)	N_{events}	Lum. (fb^{-1})
QCDbb J4 (0jets)	ALPGEN	Herwig/Jimmy	66.4	1000	0.01506
QCDbb J4 (1jets)	ALPGEN	Herwig/Jimmy	443.1	4495	0.01014
QCDbb J4 (2jets)	ALPGEN	Herwig/Jimmy	553.6	5996	0.01084
QCDbb J4 (3jets)	ALPGEN	Herwig/Jimmy	370.9	3998	0.01078
QCDbb J4 (4jets)	ALPGEN	Herwig/Jimmy	228.6	2497	0.01092
QCDbb J5+ (0jets)	ALPGEN	Herwig/Jimmy	1.3	500	0.38462
QCDbb J5+ (1jets)	ALPGEN	Herwig/Jimmy	8.5	2995	0.35236
QCDbb J5+ (2jets)	ALPGEN	Herwig/Jimmy	15.0	4990	0.33266
QCDbb J5+ (3jets)	ALPGEN	Herwig/Jimmy	14.1	4491	0.31852
QCDbb J5+ (4jets)	ALPGEN	Herwig/Jimmy	13.7	4491	0.32782
QCD J4 (2jets)	ALPGEN	Herwig/Jimmy	12,064	120832	0.01000
QCD J4 (3jets)	ALPGEN	Herwig/Jimmy	24,138	140726	0.00500
QCD J4 (4jets)	ALPGEN	Herwig/Jimmy	17,319	172373	0.00900
QCD J4 (5jets)	ALPGEN	Herwig/Jimmy	7,777	77946	0.01000
QCD J4 (6jets)	ALPGEN	Herwig/Jimmy	3,088	30920	0.01000
QCD J5+ (2jets)	ALPGEN	Herwig/Jimmy	269	80843	0.30000
QCD J5+ (3jets)	ALPGEN	Herwig/Jimmy	640	192170	0.30000
QCD J5+ (4jets)	ALPGEN	Herwig/Jimmy	625	186684	0.29800
QCD J5+ (5jets)	ALPGEN	Herwig/Jimmy	383	114819	0.29900
QCD J5+ (6jets)	ALPGEN	Herwig/Jimmy	217	29949	0.13800
QCD J2 (2jets) - filter mu10	ALPGEN	Herwig/Jimmy	27927.0	279895	0.01002
QCD J2 (3jets) - filter mu10	ALPGEN	Herwig/Jimmy	10660.9	86425	0.00810
QCD J2 (4jets) - filter mu10	ALPGEN	Herwig/Jimmy	1248.9	12500	0.01000
QCD J2 (5jets) - filter mu10	ALPGEN	Herwig/Jimmy	148.4	1500	0.01010
QCD J2 (6jets) - filter mu10	ALPGEN	Herwig/Jimmy	42.4	500	0.01180
QCD J5+ (2jets) - filter mu10	ALPGEN	Herwig/Jimmy	3004.2	29988	0.00998
QCD J5+ (3jets) - filter mu10	ALPGEN	Herwig/Jimmy	3709.0	37483	0.01010
QCD J5+ (4jets) - filter mu10	ALPGEN	Herwig/Jimmy	1224.9	12491	0.01020
QCD J5+ (5jets) - filter mu10	ALPGEN	Herwig/Jimmy	359.1	3997	0.01114
QCD J5+ (6jets) - filter mu10	ALPGEN	Herwig/Jimmy	73.1	498	0.00682

Table 4.2: *For each process of the QCD samples, the number of generated events and respective luminosity is presented.*

$p_T > 5\,\text{GeV}$ are taken into acount.

The reconstructed objects must obey specific reconstruction criteria. In the case of electrons, their reconstruction is made by the calorimeters and inner tracker of ATLAS, in the range of pseudorapidity $|\eta| < 2.47$ and transverse momentum (p_T) above 20 GeV. The isolation criterion requires that the additional transverse energy E_T in a cone of $\Delta R = 0.2$ around the electron direction be less than $(4 + 0.023E_T^{electron})\,\text{GeV}$, where $E_T^{electron}$ is the transverse energy of the electron. This isolation requirement reduces the QCD-multijet background. The range $1.37 < |\eta| < 1.52$ corresponds to the crack region of the calorimeter, within which no electron is selected.

The jet reconstruction was based on the energy deposits in calorimeter towers, with a cone algorithm of radius 0.4. The calibrated jets must be in a pseudorapidity region of $|\eta| < 5$ with a $p_T > 20\,\text{GeV}$. The jet reconstruction algorithms include both particle jet originated from electrons and from the decay of hadrons. Since some calorimeter clusters can be reconstructed as both electrons and jets, the jets within $\Delta R < 0.2$ of an electron are removed. Double counting is therefore avoided.

The muon spectrometer and the inner detector are responsible for the reconstruction of muons, by matching the spectrometer hits with the ID tracks. These leptons are required to have a p_T above 20 GeV and $|\eta| < 2.5$. Similarly to the electrons, a an isolation criteria is applied. The transverse energy in a cone of $\Delta R = 0.2$ around the muon direction is required to be less than $(0.1p_T^{\mu})$, where p_T^{μ} is the transverse momentum of the muon. The additional p_T in a $\Delta R = 0.3$ cone must be less than 4 GeV. Moreover, muons close to a jet ($\Delta R < 0.3$) are removed, reducing the selection of muons that arise from hadronic decays inside jets. No overlap removal between jets and muons that removes a jet is applied, since it is assumed that the muon released energy on the calorimeter does not give rise to the mis-reconstruction of jets.

In top quark analysis the flavour tagging of heavy jets constitutes one of the most important and useful selection criteria. The tagging of b-jets depends on the b quarks high mass and relatively long lifetime, which leads to a measurable flight of few milimeters before decaying. The tracks of such events have large impact parameters with respect to the primary vertex and

allow the reconstruction of secondary vertices. The b quark tagging tool used in the current study was the jet probability tagger, $JetProb$. The $JetProb$ is a robust algorithm, based on the impact parameter resolution function of prompt tracks. It calculates the probability for each jet to originate from a light parton. A compromise between the efficiency on the selection of the signal and the rejection of non-b processes was reached: the selected cut on the b-tag weight corresponds to 50% b-tagging efficiency and light jet rejection factor of about 120. In the future, the b-tagging algorithms will be derived from data, reducing the misstagging and achieving better preformance.

Missing transverse energy ($E_T^{missing}$) is due to: losses associated with all stable and non.interacting particles (p.e. neutrinos); and detector related losses. This last ones are due to inefficiencies and resulotion, leading to a mismeasurements of the real missing transverse energy of the objects. The missing transverse energy was calculated as the sum vector of the transverse energy deposited in the cells (either associated to the reconstructed objects or to topological clusters outside identified objects) and muons energy. Energy losses in the cryostat were also taken into account.

Chapter 5

Event Selection

In the early data period, the ATLAS performance will not be the utterly perfomance forseen by the Technical Design Report (TDR); for instance, the algorithms for the identification of isolated particles may not be optimised yet. Furthermore, it is possible that some of the backgrounds have cross sections different from the theoretical predictions. An event selection analysis at $200\,\mathrm{pb}^{-1}$ for the leptonic s-channel single top quark production, under the structure of the LipCbrAnalysis program [46, 47], is presented in this chapter. The study was divided in a sequencial and a probabilistic analysis, in order to eliminate most of the background contamination, and maximize the signal to background ratio. For this energy and luminosity, the expected data sample will lead to significant statistical errors, thus no systematic uncertainties were studied. The full simulation of the detector was used.

5.1 Single top s-channel

In the present thesis the signal is the single top s-channel, where the top is produced via a virtual W boson. The top will then decay into a W boson and a b quark through the Wtb vertex. The resulting W may decay leptonically or hadronically, but only the leptonic decay is considered as signal. The lepton can then be an electron, a muon or a tau. The taus can decay either leptonically or hadronically, however, for the present analysis, only the leponic decay of taus are considered part of signal. The analysed backgrounds

include $Wb\bar{b}$, W+jets, Z+jets, WZ pairs, QCD-multijet, $t\bar{t}$ and the other single top channels, Wt associate production and t-channel events.

The event selection was performed in two steps as described in [48]. Firstly, the events are passed through a cut based analysis (pre-selection), where the reconstructed objects were required to fulfill several kinematical and geometrical criteria. This first step of the analysis is aimed to reduce the number of background events and to select the signal events, so that a full kinematic reconstruction of the event is possible. After the preselection, a discriminant analysis (final selection), based on the probability of a given event to be signal or background-like was built. Finally, the event selection undergoes a cut on the obtained discriminant variable, reducing significantly the background contamination.

For each event, only the information about the final state particles is known, since it is the only information the detector provides. The final topology of the single top s-channel is composed by an isolated lepton (electron or muon), two b-jets and a neutrino. Due to the presence of this neutrino in the final state, the events cannot be directly reconstructed. Since the ATLAS detector cannot detect neutrinos, their reconstruction is made by requiring energy and momentum conservation in the event, given the hypothesis of signal. The neutrino four-momentum can then be estimated assuming the missing transverse energy to be the neutrino transverse momentum. However, the longitudinal component (p_{z_ν}) is still unknown. In the considered signal events, the W boson may decay into either an electron or a muon and their respective neutrino, thus:

$$p^\mu p_\mu = m_W^2 = m_l^2 + 2E_l E_\nu + 2\vec{p}_l.\vec{p}_\nu \approx 2E_l E_\nu + 2\vec{p}_l.\vec{p}_\nu \tag{5.1}$$

Since the top quark is much heavier than its decay products, the electroweak boson may be considered on-shell, with a mass $m_W = 80.4\,\text{GeV}$. Therefore, by constraining the invariant mass of the neutrino and the most energetic remaining lepton to the W mass, the longitudinal component of the neutrino momentum can be determined, with quadratic ambiguity. Assuming a negligible lepton mass, the longitudinal component of the neutrino is given by:

$$
\begin{aligned}
p_{z_\nu} &= \frac{-b \pm \sqrt{b^2 - 4ac}}{2a} \\
a &= \left(\frac{p_z^l}{E_l}\right)^2 - 1 \\
b &= 2\left(\frac{p_x^l p_x^{miss} + p_y^l p_y^{miss}}{E_l} + \frac{m_W^2}{2E_l}\right)\left(\frac{p_z^l}{E_l}\right) \\
c &= \left(\frac{p_x^l p_x^{miss} + p_y^l p_y^{miss}}{E_l} + \frac{m_W^2}{2E_l}\right)^2 - p_T^{miss\,2}
\end{aligned}
\tag{5.2}
$$

where p_i^l, with $i = x$, y, z, are the momentum components of the lepton; E_l is the lepton's energy and p_x^{miss} (p_y^{miss}) is the x (y) component of the missing momentum.

Due to the resolution of the transverse missing momentum, not all events have a solution for the neutrino longitudinal momentum. In this analysis, the chosen neutrino solution is the one with lower absolute momentum along the z-axis. This solution is in fact in most of the events, the closest to the generator value. Once the neutrino solution is established and its reconstruction implemented, the W boson reconstruction is possible.

5.2 Pre-selection

At the pre-selection level, specific criteria, matching the topology of the single top s-channel, is applied to efficiently select signal events. These cuts were applied in order to select enough signal events and reject a larger fraction of the background. The selected events are required to pass either the EF_e10_medium (electrons) or the EF_mu10 (muons) trigger, both with the lowest reconstruction p_{T} threshold.

Events are accepted if they have:

1. At least 1 isolated lepton ($p_{\mathrm{T}} > 20\,\mathrm{GeV}$ and $|\eta| < 2.5$);

2. 2 to 4 jets with a $p_{\mathrm{T}} > 20\,\mathrm{GeV}$ and $|\eta| < 5$;
3. At least 2 b-jet ($p_{\mathrm{T}} > 20\mathrm{GeV}$ and $|\eta| < 5$), with 1 high p_T b-jet ($p_{\mathrm{T}} > 30\mathrm{GeV}$);
4. $E_{\mathrm{T}}^{missing} > 20\mathrm{GeV}$;
5. Existence of a neutrino solution;
6. $m_{\mathrm{T}}^{W} > 30\mathrm{GeV}$;

The relevant normalized distributions before and after each pre-selection cut are shown in Figures 5.1, 5.2 and 5.3. Each cut was made considering the behaviour of the respective distributions and the final topology of the signal, leading to an increase of the signal to background ratio and signal significance.

As can be seen in the jet multiplicity distributions (Figure 5.2), the events with two jets are higly probable in the signal sample, whereas the major contribution to the background are events with one or less jets. The applied cut on the jet multiplicity is consistent with the top quark decays while simultaneously reduces the dilepton, the $W + 0jets$ and the QCD+$0jets$ events. The QCD multijet events are also reduced by the veto on more than 4 jets. Given the existence of at least two b-jets, the p_T distributions of the two most energetic b tagged jets are also shown in Figure 5.3. The b-tag selection reduces most of the QCD-multijet events.

Furthermore, a set of kinematic variables such as the missing transverse momentum ($E_{\mathrm{T}}^{missing}$) and the W boson transverse mass (m_{T}^{W}), turn out to be very useful to isolate the signal. The requirement of $E_{\mathrm{T}}^{missing} > 20\mathrm{GeV}$ together with the existence of the neutrino solution assure the leptonic W boson decay. The cut on the reconstructed W boson transverse mass removes most multijet background, and eliminates all of the remaining QCD multijet events. The distributions of these variables are shown in Figure 5.4.

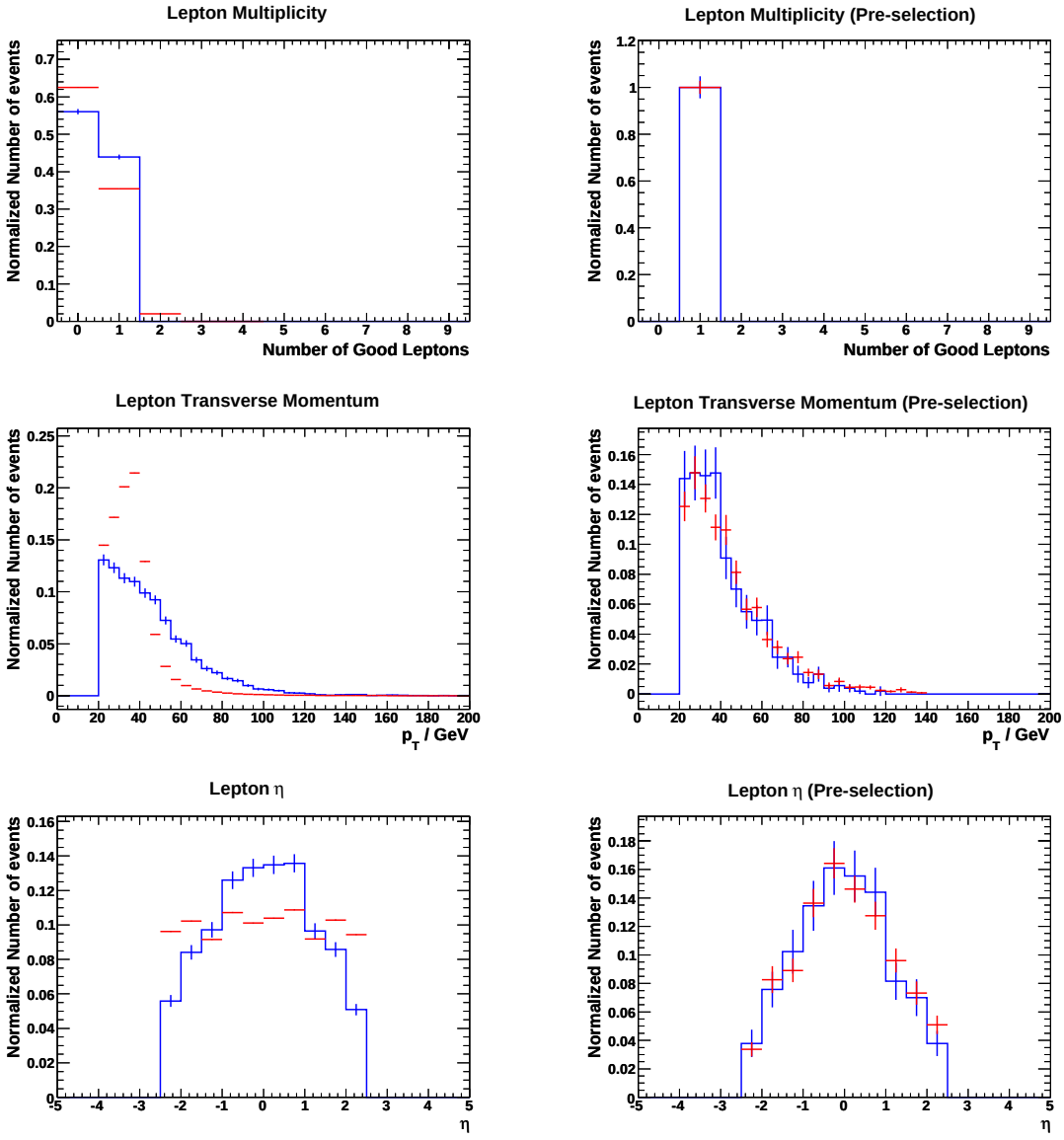

Figure 5.1: *Signal and background normalized distributions of lepton multiplicity, p_T, and psedorapidity of the lepton with highest p_T, before the first cut (left) and after all the pre-selection cuts (right). The signal is in blue and the background is in red.*

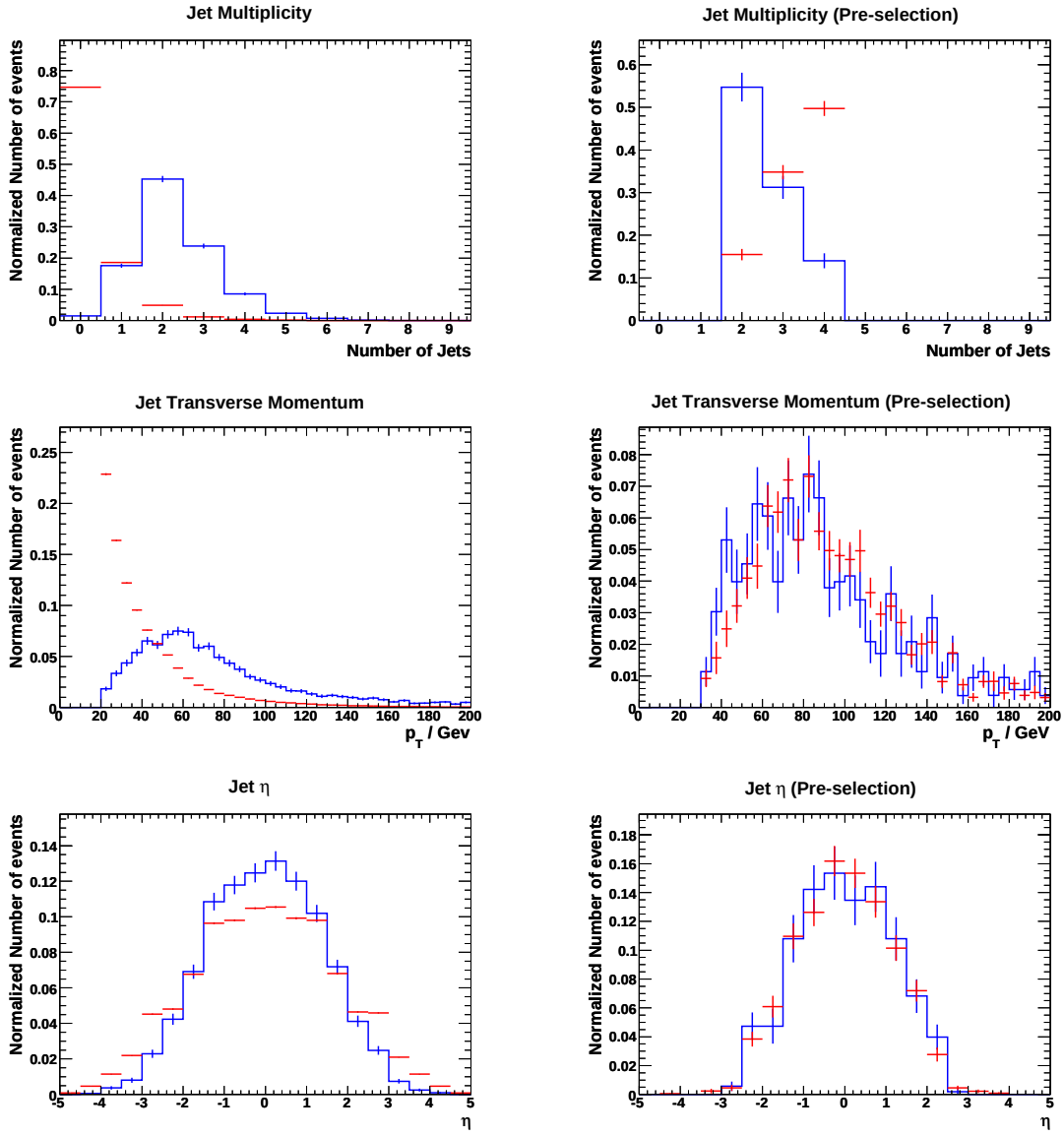

Figure 5.2: *Normalized distributions of jet (b and non-b) multiplicity, p_T, and psedorapidity of the jet with highest p_T, before the second cut (left) and after all the pre-selection cuts (right). As before, the signal is in blue and the background is in red.*

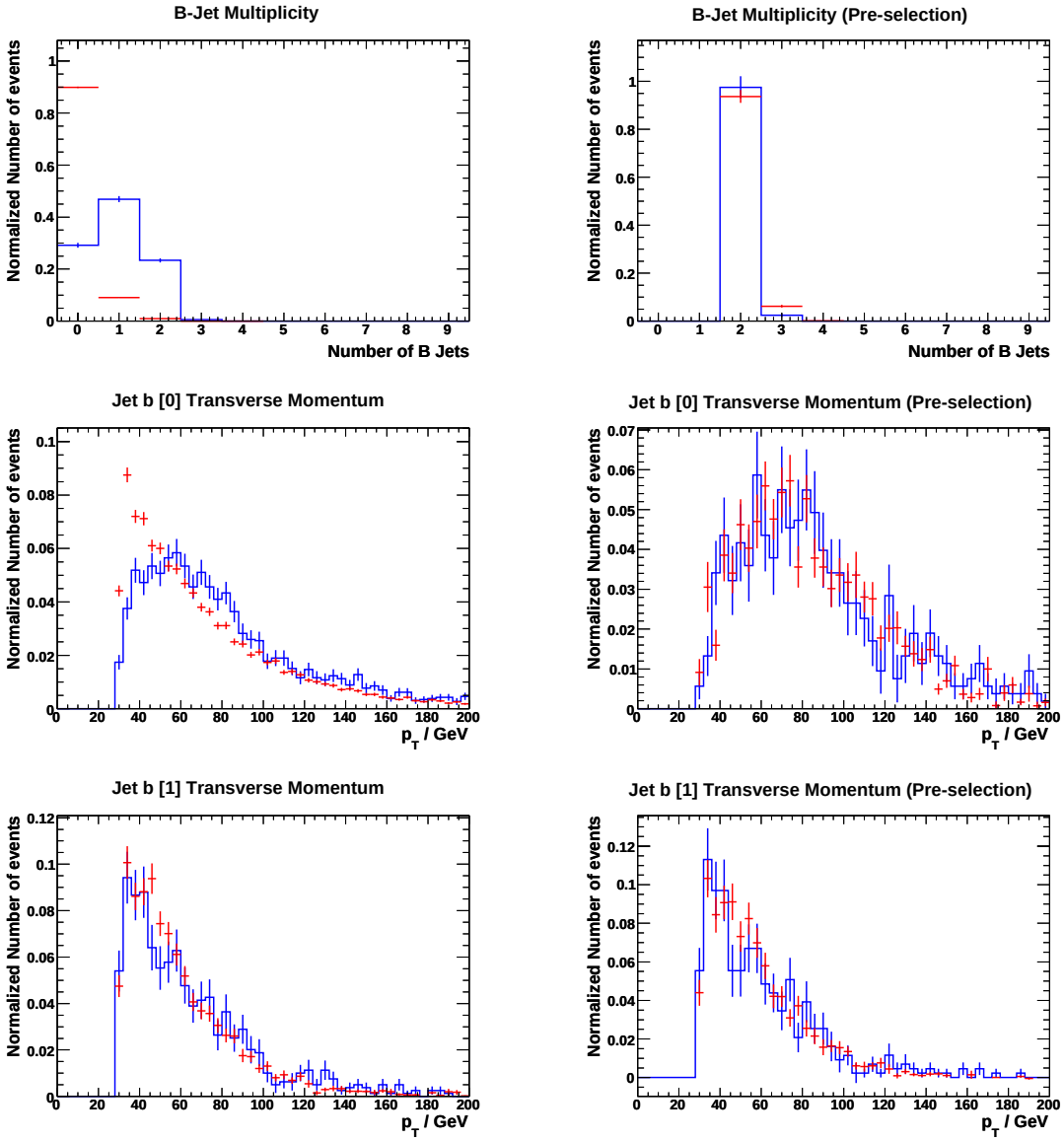

Figure 5.3: *Normalized distributions of the b-jet multiplicity and transverse momentum of the two b tagged jets with highest p_T. All the left distributions were made before the relevant cut, whereas the ones one the right are after all the pre-selection cuts. The same color code is used: blue for signal and red for background.*

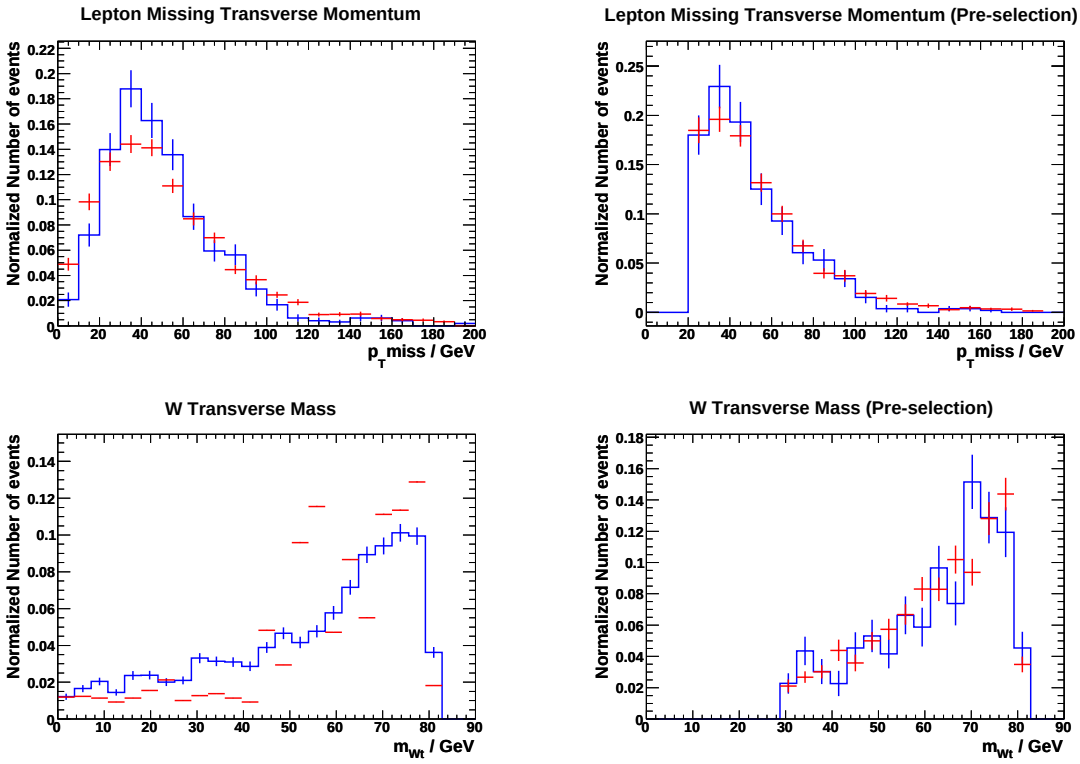

Figure 5.4: *Normalized distributions of the missing transverse momentum and the transverse W boson mass, before the cut (left) and after all cuts (right). The signal is represented in blue and the background is in red.*

Process	Pre-Selection
Single Top s-channel ($l = e, \mu$ e τ_l)	9.9 ± 0.40 ($\epsilon_s = 4.2\% \pm 0.17\%$)
Single Top (t and Wt channels)	48.0 ± 3.48
$t\bar{t}$	411.6 ± 8.96
Wbb+jactos	38.6 ± 3.00
$W(\rightarrow l\nu)$+jactos	115.7 ± 12.12
$Z(\rightarrow ll)$+jactos	3.0 ± 4.21
WW, WZ e ZZ	3.9 ± 0.19
Fundo Total	620.9 ± 16.31
S/B	1.6%
$S/\sqrt{S+B}$	0.39

Table 5.1: *Number of events after the pre-selection level normalized to a luminosity of 200* pb^{-1}*. The signal efficiency,* ϵ_s*, is also presented.*

After the pre-selection, the expected number of events for signal and backgrounds, for an integrated luminosity of $200\,\text{pb}^{-1}$, at 7 TeV is shown in Table 5.1. The dominant backgrounds are the $t\bar{t}$ and the W+jets channels. Since the signal to background ratio is 0.016, a likelihood-based analysis was developed in order to remove most of the backgrounds.

No QCD events passed the full pre-selection. Given the low Monte Carlo statistics available and the high cross sections espected for these processes, data driven techniques must be used to understand the QCD background.

5.3 Top Reconstruction

In order to fully reconstruct the top quark, the association between a b-jet and the reconstructed W boson was done. However, in the single top s-channel, there are two b-tagged jets, which lead to the reconstruction of two invariant top quark masses: one with the highest p_T b jet and the other with the second highest p_T b jet. Two different approaches were then analysed in order to reconstruct the top quark. Since the b quark from the top decay is unknown, a choice must be made between the two invariant masses, based either on a "Mass Criteria" or on a "Back-to-back Criteria". In the first method, the b-jet that reconstructs the top quark is chosen so that the top

quark mass is closer to 172.5 GeV. The top quark mass used as proximity criteria is the same used in the MC generation. The second reconstruction criteria is based on the angular distribution of the b-jet recoiling in the transverse plane against the top quark itself. Since the virtual boson decaying into a top quark is clearly off-shell, the originated b-jet will be back-to-back with the top quark, in the transverse plane. In this second approach, the chosen b-jet to reconstruct the top quark is the one whose transverse angular diference ($\Delta\phi$) with the top quark itself is higher.

In Figure 5.5, the invariant mass distribution of the reconstructed top quarks according to the two criteria is shown. For comparison purposes, it is also represented the mass distribution of the two possible top quarks (Green and Blue lines). As can be seen, the reconstructed top quark (in both criteria) does not have a preference for the most energetic b-jet. In fact, it results from an event-by-event choice between the two highest p_T b-jets. Since the "Mass Criteria" has the smallest RMS this was the criteria applied from this point forward.

The $\Delta\phi = \phi_{top} - \phi_b$ between the chosen top quark and the "recoil b" can be seen in Figure 5.6. The distribution shows that signal events lead to the top quark recoiling against the b-tagged jet, as expected.

5.4 Discriminant analysis

In order to do a discriminant analysis, seven different signal and background probability density functions (p.d.f.) were created from a set of relevant kinematical variables.

The probability, for a given event, to be signal like $\mathcal{P}_i^{signal}$ or background like $\mathcal{P}_i^{background}$ was calculated from each probability density function. A signal likelihhod can be defined as the product of the probabilities of the event to be signal,

$$\mathcal{L}_S = \prod_{i=1}^{n} \mathcal{P}_i^{signal} \tag{5.3}$$

with n = number of p.d.f. Similarly, the background likelihood is defined as

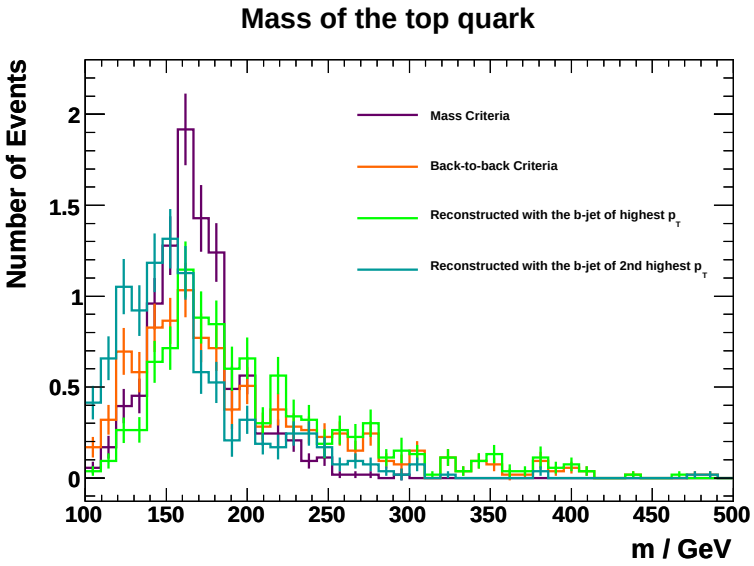

Figure 5.5: *Top mass distributions reconstructed with the highest momentum b-jet (green), the second highest momentum b-jet (blue). The distributions chosen according to the "Mass Criteria" and the "Back-to-back Criteria" are represented in purple and orange respectively.*

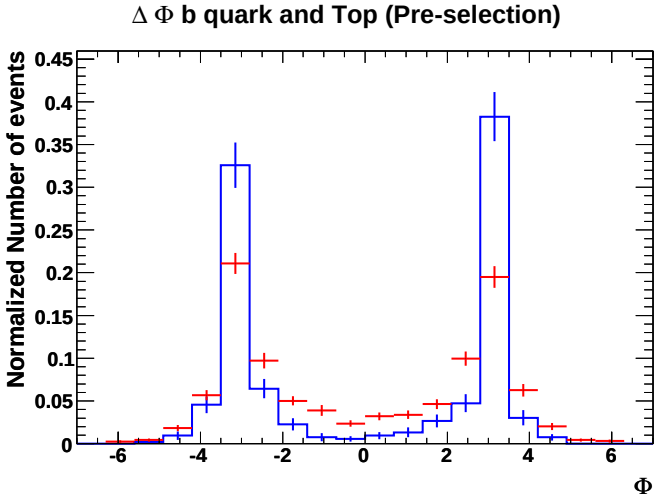

Figure 5.6: *The $\Delta\phi = \phi_{top} - \phi_b$ distribution. The signal is represented in blue and the background in red.*

$$\mathcal{L}_B = \prod_{i=1}^{n} \mathcal{P}_i^{background} \tag{5.4}$$

Having defined the Likelihoods, the discriminant variable can now be established:

$$L_R = \ln \frac{\mathcal{L}_S}{\mathcal{L}_B} \tag{5.5}$$

In order to have a good signal to background discrimination in the Likelihood ratio, the variables chosen should alternatively have different behaviours for signal and backgrounds. After the pre-selection, several probability density functions were chosen. These are shown in Figure 5.7. The list of the probability density functions used in this analysis is as follows:

- Top quark mass;
- Missing transverse momentum;
- Transverse momentum of the most energetic b (b[0]);
- Transverse momentum of the second most energetic b (b[1]);
- Transverse momentum of the isolated lepton;
- Difference in ϕ of the top quark and the recoiling b
- Cosine of the angle between the lepton and the leptonic b-jet in the Top quark rest frame.

The discriminant variable, L_R, built with these p.d.f.s, is shown in Figure 5.8. Since the signal to background ratio is higher for L_R values larger than 0.2, a cut on the likelihood ratio was applied as a last level of selection. The number of signal and background events selected is presented in Table 5.2 normalised to $L = 200\,\mathrm{pb}^{-1}$. In the final selection, the signal to background ratio (S/B) is improved from 1.6% to 3.1%, and the $t\bar{t}$ events are reduced to 52.6% of the total background. Although smaller, the W+jets is still an important background.

Process	**Final Selection**
Single Top s-channel ($l = e, \mu$ e τ_l)	6.5 ± 0.33 ($\epsilon_s = 2.7\% \pm 0.14\%$)
Single Top (t and Wt channels)	18.9 ± 2.00
$t\bar{t}$	109.7 ± 4.46
Wbb+jactos	20.6 ± 2.2
$W(\rightarrow l\nu)$+jactos	55.2 ± 9.55
$Z(\rightarrow ll)$+jactos	2.0 ± 4.09
WW, WZ e ZZ	2.3 ± 0.15
Fundo Total	208.6 ± 11.69
S/B	3.1%
$S/\sqrt{S+B}$	0.44

Table 5.2: *Events at final selection level normalized to* $L = 0.200\,\mathrm{fb}^{-1}$. *The signal efficiency,* ϵ_s, *is also shown.*

There are other multivariate techniques intended to optimize the discrimination between signal and backgrounds. Unlike the Likelihood method, their success depends greatly on the correlations between the variables used.

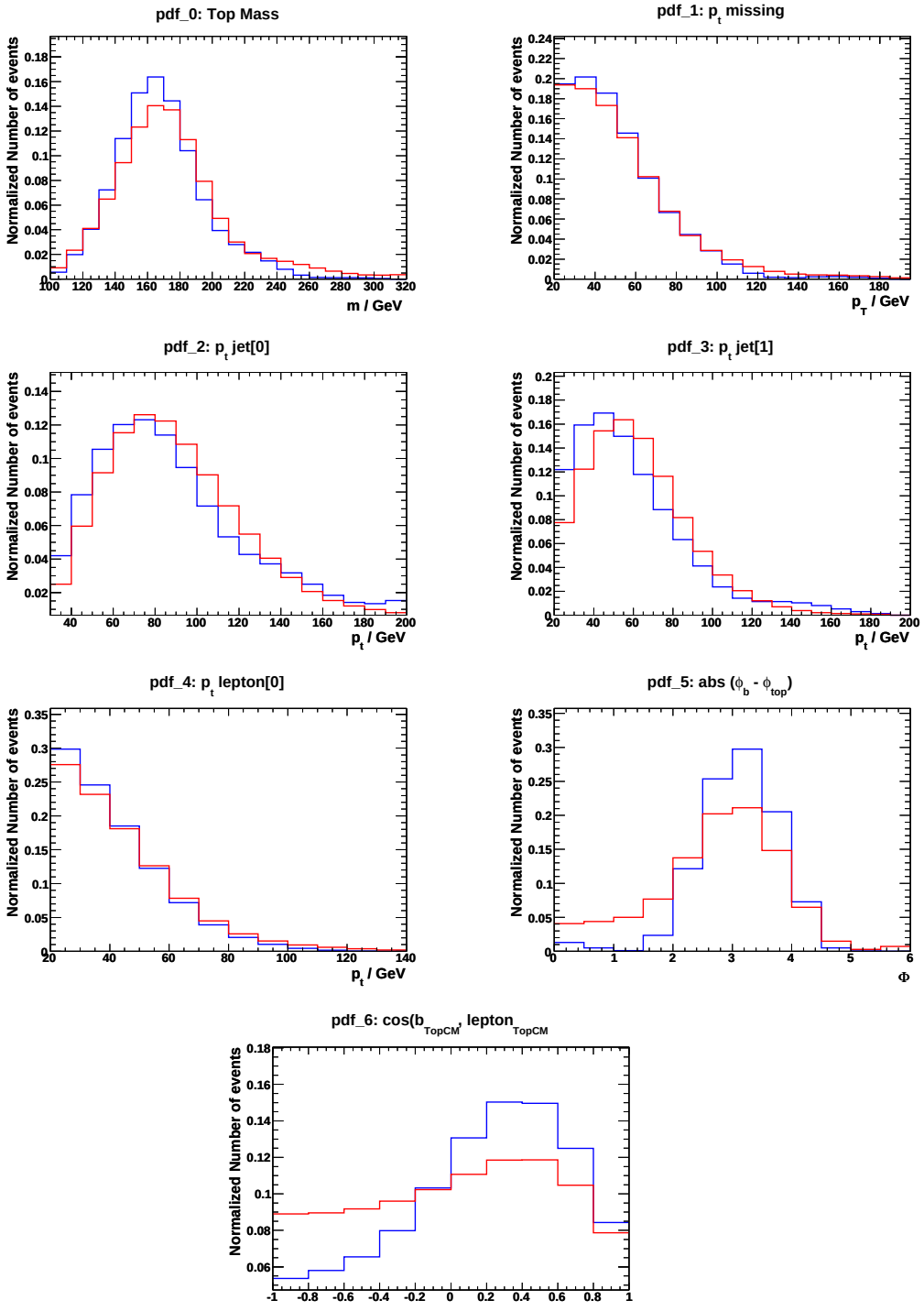

Figure 5.7: *Probability density functions for signal (blue) and background (red).*

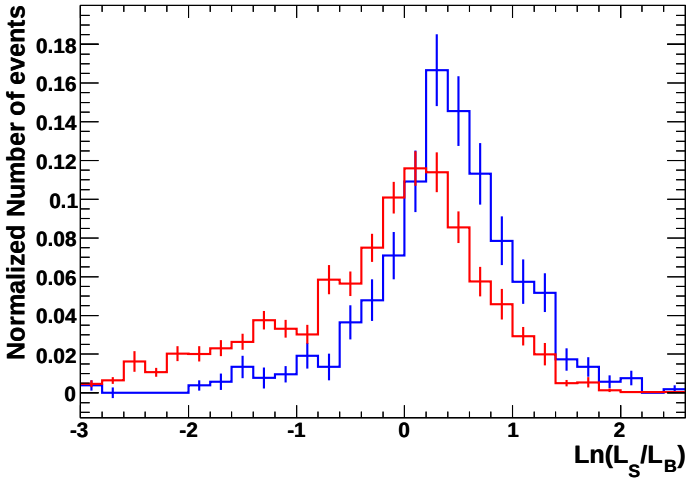

Figure 5.8: *Likelihood ratio for signal (blue) and background (red).*

Chapter 6

Results

In this chapter, the determination of the single top s-channel cross section is presented, as well as its statistical uncertainty.

6.1 Cross Section

In order to measure the cross section of the single top s-channel, an estimate of the signal events in a fake data sample must be made. Therefore, two independent and equivalent simulated samples of signal and background are used: (S_1, B_1) and (S_2, B_2). With the first samples a fake data sample is created $D_1 = S_1 + B_1$, and no access to the individually S_1 and B_1 is possible. Consequently, the S_2 and B_2 are the reference samples, on which the analysis presented on Chapter 5 was developed.

To estimate the number of signal events after the full selection, the background estimate (B_2) is subtracted from the fake data sample:

$$N = D_1 - B_2 \tag{6.1}$$

The number of signal events for a given physics process can be estimated by knowing the process cross section (σ), the integrated luminosity (L) and the analysis signal efficiency (ϵ):

$$N = \sigma L \epsilon \tag{6.2}$$

After the final selection, a cross section measurement can be performed

if the number of events, the signal efficiency and the integrated luminosity are known, i.e.,

$$\sigma_s = \frac{D_1 - B_2}{L\epsilon} \tag{6.3}$$

The theoretical NLO value of the s-channel is 3.94 pb. The MC samples used were simulated with a production cross section of 1.4069 pb because only leptonic W decays are included. Therefore, the branching ratio of this decay ($BR = 32.57\%$) has to be included in the cross section determination:

$$\sigma_s = \frac{D_1 - B_2}{L\epsilon BR} \tag{6.4}$$

From the signal reference sample, S_2, the selected efficiency can be obtained dividing the number of events that pass the analysis full selection by the number of events in the generated sample.

$$\epsilon = \frac{S_2(\text{after all selection cuts})}{S_2(\text{generator level})} \tag{6.5}$$

The obtained value is $\epsilon_s = (2.7 \pm 0.14) \times 10^{-2}$, as already shown in Table 5.2. Both the selection efficiency and the trigger efficiency contribute to ϵ_s. The geometrical acceptance of the detector is also included in the signal efficiency.

The σ_s precision depends on both statistical and systematical errors. The statistical error associated with the cross section measurement, according to equation (5.3), is given by:

$$\frac{\delta\sigma_s}{\sigma_s} = \frac{\delta N}{N} \oplus \frac{\delta L}{L} \oplus \frac{\delta\epsilon_s}{\epsilon_s} \tag{6.6}$$

where the δN, δL and $\delta\epsilon_s$ are the statistical uncertainties in the number of events, integrated luminosity and signal efficiency respectively. The systematic uncertainty determination would be the next natural step. These are related to detector uncertainties, such as particle identification efficiencies, background rejections or energy scales and resolutions. For instance, the Jet Energy scale, the b-tagging efficiency and the pile up effect, all are sources of uncertainty, affecting cross section measurements as well as background estimates. These uncertainties can be constrained and minimized with a

better knowledge of the detector. On the early data taking period, the error on the luminosity determination is estimated to be around 10%. Due to the approximations made by the Monte Carlo generators other systematic uncertainties must also be taken into acount. In particular, the scale dependence of the cross section calculations, the parton distribution functions and the top quark mass experimental error.

Result

At 7 TeV the cross section of the s-channel is calculated, considering an integrated luminosity of $L = 200\,\mathrm{pb}^{-1}$. The obtained result is presented in Table 6.1. Only statistical uncertainties were considered and the luminosity uncertainty was was not included in the cross section error.

Given the lower number of expected signal events for an integrated luminosity of $200\,\mathrm{pb}^{-1}$ at 7 TeV, large statistical uncertainties are predicted. The cross section value was obtained at 1σ, due to the low statistics available at the considered energy and luminosity. Thus, the determination of systematic uncertainties is not yet useful. Nevertheless, this result suggests the importance of the estimation of major backgrounds, from data-driven methods. In particular, for high cross section processes, where the generation of sufficient MC simulated events is not possible, the data-driven estimation assumes an important role.

D_1	B_2	ϵ_s	σ_s	$\Delta\sigma_s/\sigma_s$
224.8 ± 11.53	208.6 ± 11.69	$(2.7 \pm 0.14) \times 10^{-2}$	$9.06 \pm 9.19\,\mathrm{pb}$	1.015

Table 6.1: *Number of events on the fake data and background reference samples, signal efficiency, measured cross section and its precision, for a luminosity of* $L = 200\,\mathrm{pb}^{-1}$ *at* $\sqrt{s} = 7\,\mathrm{TeV}$.

Limits on the cross section

Due to the low statistics available at 7 TeV a cross section limit at 95% confidence level (CL) can be derived, assuming absence of signal events. With

data, these upper limits on the number of signal events for each channel can be determined by fitting the discriminant variables obtained from the data events with those for the hypothesis of signal plus background, without doing any cuts on the distributions. Since no data was analysed, the background sample B_1 was used as fake data. In order to fit the discriminant variables obtained from the fake data events with those of signal plus background $(S_2 + B_2)$, a test-statistic was done:

$$X_d = \sum_i n_i \ln\left(1 + \frac{s_i}{b_i}\right) \tag{6.7}$$

where i is the number of bins of all discriminant variables, and n_i, s_i and b_i are the number of events in bin i of the discriminant variables in the fake data, the expected background and the signal events, respectively. Larger values of X_d evidence the similarity between the signal and the data samples.

Similar statistical tests were obtained for the signal plus background hypotheses (X_{s+b}) and background only (X_b). The X_{s+b} distribution was determined iteratively, through the simulation of statistically compatible distributions with the sum of the signal and the background discriminant variables, according to the Poisson distributions. In each iteraction, X_{s+b} was calculated as:

$$X_{s+b} = \sum_i n_i^{s+b} \ln\left(1 + \frac{s_i}{b_i}\right) \tag{6.8}$$

where n_i^{s+b} is the total number of events of the discriminant variables in the signal plus background sample. The test-statisc of background only was performed in a similar fashion:

$$X_b = \sum_i n_i^{b} \ln\left(1 + \frac{s_i}{b_i}\right) \tag{6.9}$$

where n_i^b is the total number of events in the simulated distributions of the background discriminant variables.

In the modified frequentist likelihood method, the CL of the extracted limit is defined as [47]:

$$1 - CL = \frac{\int_0^{X_d} P_{s+b}(X)dX}{\int_0^{X_d} P_b(X)dX} \tag{6.10}$$

where P_{s+b} and P_b are the X_{s+b} and X_b distributions, respectively. The discriminant variables used were the likelihoods obtained on the previous chapter: the S_2 and B_2 samples constitute the signal and background hypotheses, whereas sample B_1 is the fake data. The cross section expected limit at 95%CL is the value for which equation 6.10 is equal to 0.05 and is obtained assuming the fake data events are perfectly described by the expected background. The median of the statistical test was computed by replacing X_d with the median of the statistical test for the background hypothesis (X_b).

Using the likelihood distributions, a limit was set at 95% CL, assuming no signal event passes the sequential analyses. The same values of luminosity, branching ratio and signal efficiency were used (see Table 6.1). The obtained value for the cross section expected limit is represented in Table 6.2.

-1σ	expected	$+1\sigma$
47 pb	66 pb	91 pb

Table 6.2: *The expected* 95% *confidence level limits on the single top s-channel production in the absence of signal hypothesis, are shown. The central values are presented together with the* 1σ *bands, which include the contribution from the statistical uncertainties.*

Chapter 7

Conclusions

In this thesis, the ATLAS sensitivy to the leptonic s-channel single top quark production was studied. Considering the leptonic topology as signal, the value of the cross section was calculated for a luminosity of $200\,\mathrm{pb}^{-1}$. Due to its large statistical error, an expected limit at 95% CL on the cross section of the s-channel prodution, in the absence of signal, was established.

The analysed events were generated through Monte Carlo techniques and the full simulation of the ATLAS detector was used, providing a detailed description of the detector geometry and reconstruction algorithms. The signal event selection was developed in two levels: a sequential and a discriminant analysis. These selection criteria were applied in order to reduce significantly the number of background events and effectively select the signal. After the sequential analysis no QCD multijet events survived and the major backgrounds were $t\bar{t}$ (66.3%) and W+jets (18.6%). The $t\bar{t}$ process can be isolated in other decay modes and in principle will be well measured. The discriminant analysis significantly reduced the background events, without much deterioration of the signal efficiency. The signal to background ratio was incresased after the likelihood cut and the background is reduced by about 66%. Moreover, the reconstruction of the top quark was made using different methods: either a mass proximity criteria or an angular criteria.

After the final selection, the cross section value of the s-channel and its statistical uncertainty were estimated. At 7 TeV, and with a luminosity of $200\,\mathrm{pb}^{-1}$, the obtained value was $\sigma_s = 9.06 \pm 9.19\,\mathrm{pb}$. The cross section

measurement was made with a statistical precision of $\frac{\Delta\sigma}{\sigma} = 1.01$. Due to this large statistical uncertainty, no systematic error was studied. However, since large statistics samples will be achieved at the LHC, the systematic uncertanties are expected to be of major importance in the higher luminosity periods.

From the selection analysis, a limit on the cross section value was determined with 95% CL, through the use of the modified frequentist likelihood method. The observed limit was $\sigma_s < 66\,\text{pb}$ for the s-channel of single top quark production. The obtained limit can be improved if a better estimation of the background is made, for instance, via data-driven methods.

In short, during the early data taking no precise measurement of the s-channel cross section can be made. Nevertheless, the study of the background behaviour is of major importance. From this analysis, the dominant backgrounds are expected to be $t\bar{t}$ and W+jets events, whose detailed comprehension is still unknown. At 7 TeV, and with an increasing luminosity, the s-channel might be observed at LHC as long as the background estimation is improved. Consequently, an increase of statistics and the use of background estimation through data based methods will lead to an improvement on the signal to background ratios, allowing a measurement of the single top s-channel cross section.

At the LHC, top quark physics is one of the main fields of study. With the rapid luminosity improvement, it will soon be producing top quarks at daily basis. As one of the main LHC experiments, the ATLAS detector will contribute to the top quark rediscovery and to the study of its properties. The observation of the pair production process will be possible with just a few tens of pb^{-1} and with a few hundred more the electroweak single top production should already be detected. The top quark properties are expected to be examined with significant precision at the LHC, contemplating entirely new measurements on the basis of the large available statistics. However, better understanding of QCD dynamics and other relevant backgrounds is required to make full use of the rich statistics of top quark events.

In conclusion, the top quark has opened a rich field of physics, not only due to its interesting properties, which will be a test to the standard model, but also because the top quark may lead to the discovery of new physics. Its

large mass may well indicate a special role in electroweak symmetry breaking and particles yet unobserved may show up in its production or decay. Standard Model deviations may occur on anomalous couplings of the Wtb vertex or on a non unitary value of the $|V_{tb}|$, indicating the existence of a heavy fourth quark family. Thus, top quark physics is the perfect area for the search of new physics effects. Nonetheless, careful measurements of the top quark production and decay characteristics, and precision measurement of its mass and other properties, are needed in order to test the Standard Model and constrain the mass of the Higgs boson. Finally, since top quark events will constitute a strong background to many potential new physics searches, their knowledge is of extreme importance.

Bibliography

[1] F. Abe et al. Observation of top quark production in $\bar{p}p$ collisions. *Phys. Rev. Lett.*, 74:2626–2631, 1995.

[2] S. Abachi et al. Observation of the top quark. *Phys. Rev. Lett.*, 74:2632–2637, 1995.

[3] Makoto Kobayashi and Toshihide Maskawa. CP Violation in the Renormalizable Theory of Weak Interaction. *Prog. Theor. Phys.*, 49:652–657, 1973.

[4] V. M. Abazov et al. Search for single top quark production in p anti-p collisions at $\sqrt(s) = 1.96$ TeV. *Phys. Lett.*, B622:265–276, 2005.

[5] T. Aaltonen and others (CDF Collaboration). Measurement of the Single Top Quark Production Cross Section at CDF. 2008, arXiv:0809.2581 [hep-ex].

[6] C. Amsler and others (Particle Data Group). Review of particle physics. *Phys. Lett.*, B667:1, 2008.

[7] S. L. Glashow. Partial Symmetries of Weak Interactions. *Nucl. Phys.*, 22:579–588, 1961.

[8] Abdus Salam. Weak and Electromagnetic Interactions. Originally printed in *Svartholm: Elementary Particle Theory, Proceedings Of The Nobel Symposium Held 1968 At Lerum, Sweden*, Stockholm 1968, 367-377.

[9] Steven Weinberg. A Model of Leptons. *Phys. Rev. Lett.*, 19:1264–1266, 1967.

[10] Arnulf Quadt. Top quark physics at hadron colliders. *Eur. Phys. J.*, C48:835–1000, 2006.

[11] Steven Weinberg. The quantum theory of fields. Vol. 2: Modern applications. Cambridge, UK: Univ. Pr. (1998).

[12] Peter W. Higgs. Broken symmetries, massless particles and gauge fields. *Phys. Lett.*, 12:132–133, 1964.

[13] Peter W. Higgs. Spontaneous Symmetry Breakdown without Massless Bosons. *Phys. Rev.*, 145:1156–1163, 1966.

[14] S. Fukuda et al. Determination of Solar Neutrino Oscillation Parameters using 1496 Days of Super-Kamiokande-I Data. *Phys. Lett.*, B539:179–187, 2002.

[15] Nicola Cabibbo. Unitary symmetry and leptonic decays. *Phys. Rev. Lett.*, 10(12):531–533, Jun 1963.

[16] Tevatron Electroweak Working Group for the CDF and D0 Collaborations. Combination of CDF and D0 Results on the Mass of the Top Quark. 2009, hep-ex/0903.2503v1.

[17] Werner Bernreuther. Top quark physics at the LHC. *J. Phys.*, G35:083001, 2008.

[18] Roberto Bonciani, Stefano Catani, Michelangelo L. Mangano, and Paolo Nason. NLL resummation of the heavy-quark hadroproduction cross-section. *Nucl. Phys.*, B529:424–450, 1998.

[19] V. M. Abazov et al. Evidence for production of single top quarks. *Phys. Rev.*, D78:012005, 2008.

[20] R. Hawkings U. Husemann S. Allwood-Spiers L. Mijovic B. Kersevan G. Khoriauli N. F. Castro A. Lucotte J. Donini C. Feng W. Verkerke L. Fiorini S. Grinstein A. Gaponenko D. Whiteson B. Cooper A. Messina M. Gosselink N. Vlasov A. Shibata, M. Bosman and M. Cristinziani. Understanding Monte Carlo Generators for Top Physics, Tech. Rep. 2009. ATL-COM-PHYS-2009-334.

[21] B. Clément et al. Prospect for single top cross-section measurements in ATLAS. 2009.

[22] Zack Sullivan. Understanding single-top-quark production and jets at hadron colliders. *Phys. Rev.*, D70:114012, 2004.

[23] John Campbell and Francesco Tramontano. Next-to-leading order corrections to W t production and decay. *Nucl. Phys.*, B726:109–130, 2005.

[24] CDF Colaboration. A Limit on the Top Quark Width and Lifetime using the Template Method in the Lepton plus Jets Channel at CDF II. *CDF Note*, 8953, 2007.

[25] J. A. Aguilar-Saavedra, J. Carvalho, Nuno Filipe Castro, Filipe Veloso, and A. Onofre. Probing anomalous W t b couplings in top pair decays. *Eur. Phys. J.*, C50:519–533, 2007.

[26] J. A. Aguilar-Saavedra. A minimal set of top anomalous couplings. 2008, arXiv:0811.3842 [hep-ph].

[27] Gregory Mahlon and Stephen J. Parke. Single top quark production at the LHC: Understanding spin. *Phys. Lett.*, B476:323–330, 2000.

[28] J. A. Aguilar-Saavedra. Single top quark production at LHC with anomalous Wtb couplings. *Nucl. Phys.*, B804:160–192, 2008.

[29] J. A. Aguilar-Saavedra et al. Study of ATLAS sensitivity to asymmetries in single top events. *Nuovo Cim.*, 123B:1323–1324, 2008.

[30] Miguel Castro Nunes Fiolhais. Study of ATLAS sensitivity to asymmetries in single top events. CERN-THESIS-2009-014.

[31] Oliver S. Bruning, (Ed.) et al. LHC design report. Vol. I: The LHC main ring. CERN-2004-003-V-1.

[32] F. Seyvet et al. Long term stability of the LHC superconducting cryodipoles after outdoor storage. Prepared for MT-19: 19th International Conference on Magnet Technology, Genoa, Italy, 18-23 Sep 2005.

[33] : G. Aad et al. Expected Performance of the ATLAS Experiment - Detector, Trigger and Physics. 2009.

[34] G. Aad et al. The ATLAS Experiment at the CERN Large Hadron Collider. *JINST*, 3:S08003, 2008.

[35] ATLAS: Detector and physics performance technical design report. Volume 1. CERN-LHCC-99-14.

[36] A. Yamamoto et al. The ATLAS central solenoid. *Nucl. Instrum. Meth.*, A584:53–74, 2008.

[37] ATLAS high-level trigger, data acquisition and controls: Technical design report. CERN-LHCC-2003-022.

[38] R. W. L. Jones. ATLAS computing and the GRID. *Nucl. Instrum. Meth.*, A502:372–375, 2003.

[39] S. Agostinelli et al. GEANT4: A simulation toolkit. *Nucl. Instrum. Meth.*, A506:250–303, 2003.

[40] Eric S. Swanson. Aspects of confinement: A brief review. *AIP Conf. Proc.*, 717:636–645, 2004.

[41] G. Corcella et al. HERWIG 6.5: an event generator for Hadron Emission Reactions With Interfering Gluons (including supersymmetric processes). *JHEP*, 01:010, 2001.

[42] S. Lloyd. Atlas computing work book.

[43] Stefano Frixione and Bryan R. Webber. Matching NLO QCD computations and parton shower simulations. *JHEP*, 06:029, 2002.

[44] Michelangelo L. Mangano, Mauro Moretti, Fulvio Piccinini, Roberto Pittau, and Antonio D. Polosa. ALPGEN, a generator for hard multiparton processes in hadronic collisions. *JHEP*, 07:001, 2003.

[45] Matteo Cacciari, Gavin P. Salam, and Gregory Soyez. The anti-kt jet clustering algorithm. *JHEP*, 04:063, 2008.

[46] Nuno Filipe da Silva Fernandes de Castro. Study of the Wtb vertex structure at the ATLAS experiment. CERN-THESIS-2008-083.

[47] Filipe Manuel Almeida Veloso. Study of ATLAS sensitivity to FCNC top quark decays. CERN-THESIS-2008-106.

[48] B Clement, J Donini, C Feng, D Hirschbuehl, A LlÃ¨res, A Lucotte, M ZurNedded, P Ryan, P Sturm, W Wagner, and J Wang. Strategy to search for single-top events using early data of the atlas detector at the lhc. Technical Report ATL-COM-PHYS-2010-093, CERN, Geneva, Feb 2010.